International Journal of Pharmaceutics 668 (2025) 124997

Contents lists available at ScienceDirect

International Journal of Pharmaceutics

journal homepage: www.elsevier.com/locate/ijpharm

Heme oxygenase 1 inhibitor discovery and formulation into nanostructured lipid carriers as potent and selective treatment against triple negative metastatic breast cancer

Nicola Filippo Virzì [a,b], Carmen Alvarez-Lorenzo [b], Angel Concheiro [b], Valeria Consoli [a], Loredana Salerno [a], Luca Vanella [a], Valeria Pittalà [a,c,*], Patricia Diaz-Rodriguez [b,*]

[a] Department of Drug and Health Science, University of Catania, Catania 95125, Italy
[b] Departamento de Farmacología, Farmacia y Tecnología Farmacéutica, I+D Farma (GI-1645), Faculty of Pharmacy, iMATUS, and Health Research Institute of Santiago de Compostela (IDIS), Universidade de Santiago de Compostela, Santiago de Compostela 15782, Spain
[c] Department of Molecular Medicine, Arabian Gulf University, Manama 329, Bahrain

ARTICLE INFO

Keywords:
Heme Oxygenase-1 (HO-1) inhibitor
Nanostructured lipid carriers (NLC)
Metastatic cancer treatment
Melanoma
Triple negative breast cancer (TNBC)
Selective targeting
In ovo antitumoral test

ABSTRACT

Heme oxygenase-1 (HO-1) has been identified as a potential new target in anticancer therapy, being overexpressed in different tumors and crucial for cell proliferation. Advances in the development of specific HO-1 inhibitors should support the understanding of controlling HO-1 activity as antitumoral strategies, opening the path for future therapeutic applications. In the present study, small series of new HO-1 inhibitors were synthesized by joining a butylimidazolic pharmacophore together with a hydrophobic moiety spaced by a 2-oxybenzamide central linker. The most active and selective HO-1 inhibitor, VP 21–04, 2-(4-(1*H*-imidazol-1-yl) butoxy)-*N*-benzyl-5-iodobenzamide (7b) was identified. This ligand showed strong cytotoxic activity against melanoma and breast cancer cell lines. Encapsulation of VP 21–04 in nanostructured lipid carriers (NLC 21–04) was performed to exploit its therapeutic potential by passive-targeting delivery ameliorating water-solubility and toxicity. Interestingly, NLC 21–04 showed a marked antiproliferative effect in both cancer cell lines, and an improved safety profile with a wider therapeutic window when compared to the free drug. Finally, NLC 21–04 showed a marked tumor growth reduction while being safe in an *in ovo* tumor model, highlighting the therapeutic potential of the developed nanoparticles against triple negative metastatic breast cancer.

1. Introduction

Heme Oxygenase (HO) is a family of enzymes devoted to heme catabolism. Through its enzymatic activity, the pro-oxidant heme molecule is converted into equimolar amounts of Fe^{2+} and two cytoprotective catabolites, carbon monoxide (CO) and biliverdin (BV) (Abraham and Kappas, 2008). Two main HO isoforms have been identified in humans nowadays, possessing similar aminoacidic sequences (55 % of identity and 76 % of similarity) (Yi and Ragsdale, 2007). However, the two isoforms differ in their tissue distribution and mechanism of induction (Floresta et al., 2021a; Kutty et al., 1994). Heme oxygenase-1 (HO-1), also known as heat shock protein 32 (Hsp32), presents strong cytoprotective roles. This protein is located at the endoplasmic reticulum and principally distributed in spleen, liver, and bone marrow under basal conditions. However, its induction in other tissues can be triggered by the activation of the Nrf2/Keap-1 axis as a stress stimuli response to cell-damaging factors, such as oxidative stress, drugs, heavy metals, UV radiation, and high heme concentration (Dennery, 2014). In contrast, Heme Oxygenase-2 (HO-2) is a constitutive isoform present in testis and brain, where, through CO production and consecutive vasodilatation, seems to have a role in neuroprotection and male reproduction (Intagliata et al., 2019; Maines, 1997).

During the last decades the cytoprotective, antioxidant, and detoxifying role of HO-1 in normal cells has been elucidated, while its involvement in tumors development, spreading and metastatisis still requires further understanding. Several studies pointed out how HO-1

* Corresponding authorsat: Department of Drug and Health Science, University of Catania, Catania 95125, Italy (V. Pittalà). Departamento de Farmacología, Farmacia y Tecnología Farmacéutica, I+D Farma (GI-1645), Faculty of Pharmacy, iMATUS, and Health Research Institute of Santiago de Compostela (IDIS), Universidade de Santiago de Compostela, 15782 Santiago de Compostela, Spain (P. Diaz-Rodriguez).
E-mail addresses: valeria.pittala@unict.it (V. Pittalà), patricia.diaz.rodriguez@usc.es (P. Diaz-Rodriguez).

https://doi.org/10.1016/j.ijpharm.2024.124997
Received 21 September 2024; Received in revised form 17 November 2024; Accepted 21 November 2024
Available online 23 November 2024

overexpression in different solid and liquid tumors leads to heightened aggressiveness, abnormal proliferation, and angiogenesis induction (Grochot-Przeczek et al., 2014; Na and Surh, 2014; Nitti et al., 2017; Wegiel et al., 2014). Moreover, the involvement of HO-1 in the immune evasion of cancer cells further decreases patient survival rate (Kozakowska et al., 2012; Pae et al., 2003; Seo et al., 2015). Increasing evidence suggests the cytoprotective role exerted by HO-1 in tumor cells could affect the efficacy of antitumoral drugs. A clear example is given by the overexpression of HO-1 in chronic myeloid leukaemia cells (CML), which leads to chemoresistance to imatinib (Schaefer and Behrends, 2017). The same effect was noticed in acute myeloid leukaemia (AML) and multiple myeloma (MM), in which the high expression of HO-1 causes cytarabine, daunorubicin (for AML), and arsenic trioxide (for MM) treatments failure (Heasman et al., 2011; Morales et al., 2009).

Previously published data have already reported the ability of small molecules HO-1 inhibitors in reducing several tumoral cell lines viability (Fallica et al., 2021; Greish et al., 2018b; Mucha et al., 2019; Salerno et al., 2015). Nevertheless, even if HO-1 inhibitors may have promising *in vitro* cytotoxic activity, the field is relatively new and further investigations are needed to unravel the role of HO-1 in tumors and the effect of its selective blockade, by new potent and selective inhibitors, on tumor growth. The selectivity of such inhibitors between the two isoforms is always preferred to not impair the physiological process where HO-2 is involved and avoid undesired adverse side effect in non-target sites (Maines, 1997).

To fully profit from the therapeutic potential of novel chemical compound, the combination with an appropriate nanoparticle formulation may be an efficient strategy to pursue. It is well known how lipid-based formulations can improve the performance and some aspects of the ADMET profile of lipophilic drugs, such as bioavailability, passive targeting, clearance, and toxicity. Among them, NLC, a blend of solid and liquid lipids, have proved to be the most promising one, overcoming the drawbacks of liquid emulsions (LE) and solid lipid nanoparticles (SLN) such as the physical instability, limited loading capacity, expulsion of the drug from the formulation or needs of high surfactant concentrations that can give toxicity Indeed, NLC usually require low surfactant content and possess low toxicity, as well as high drug solubilization ability for lipophilic drugs with high encapsulation efficiency and long-term stability (Khan et al., 2015).

Thus, the present work aims at a dual objective: (i) design and synthesize novel HO-1 inhibitors taking inspiration from our previously developed compounds to ameliorate potency and HO-1 selectivity, while decreasing the activity over HO-2 (Floresta et al., 2021b; Salerno et al., 2013); (ii) encapsulate the identified most potent and selective HO-1 inhibitor in nanostructured lipid carriers (NLC) to enhance drug solubility and efficacy while decreasing toxicity and possible side effects (Alghamdi et al., 2022).

Hence, the combination of potent and selective HO-1 inhibitors with an appropriate NLC formulation can be a promising strategy to fully exploit the therapeutic potential of this category of smalls drug for cancer therapy.

To carry out the work, the novel inhibitors were synthesized, characterized, and screened for HO-1 and HO-2 inhibition. The most potent compound was then tested in the NCI-60 tumoral cell panel by the National Cancer Institute (NCI, Bethesda, MD, USA) (Shoemaker, 2006). After identifying the tumoral cell targets, NLC loaded with HO-1 inhibitor were formulated and extensively characterized by dynamic light scattering (DLS), UV–vis spectroscopy, and Transmission Electron Microscopy (TEM). *In vitro* antiproliferative tests were conducted on melanoma (SK-MEL-5) and triple-negative breast cancer (TNBC) (MDA-MB-468) cell lines. In parallel, cytocompatibility tests on fibroblast (BALB/3T3) were performed. Finally, an *in ovo* testing on TNBC tumors was performed as an *in vivo* alternative suitable model to further evaluate the antitumoral activity of the developed NLC in an environment that resembles the tumoral 3D structure.

2. Materials and methods

2.1. Materials

Labrasol ALF and Compritol ATO 888 were a kind gift from Gattefosse, Saint-Priest, France. Tween® 80, DMSO, and Lecithin were obtained from Sigma Aldrich (St Louis, MO, USA). Dulbecco's Modified Eagle Medium (DMEM), Eagle's minimal essential medium (EMEM), Gibco™ Antibiotic-Antimycotic (anti-anti), Fetal Bovine Serum (FBS), TryplE®, Alamar Blue™, Dulbecco's phosphate buffer saline (DPBS) and CellTracker™ Green 5-chloromethylfluorescein diacetate (CMFDA) was obtained from ThermoFisher Sci (Waltham, MA, USA). Matrigel™ was purchased from Corning (Corning, NY, USA). All the remaining chemicals and solvents were reagent grade and purchased from commercial sources.

2.2. Chemistry

A CEM Discover microwave synthesizer (CEM, Matthews, NC, USA) using closed Pyrex glass tubes with Teflon-coated septa was used to carry out the microwaves assisted reactions. Reactions were monitored on TLC aluminium sheets coated with silica gel (60 F254, Merck, Kenilworth, NJ, USA) and visualized by UV ($\lambda = 254$ and 366 nm) and iodine chamber. For the purification of the compounds flash chromatography was performed on glass columns employing silica gel (Merk 60, 0.040–0.063 mm, 230–400 mesh) as stationary phase. The infrared spectra of the obtained molecules were recorded on a Perkin Elmer 281 FTIR spectrometer (Perkin Elmer, Waltham, MA, USA) using KBr disks or NaCl plates. Melting points were determined in capillary glass tubes in an IA9200 Electrothermal (Electrothermal Engineering Ltd, Sutton, Essex, UK) apparatus equipped with a digital thermometer, and depicted uncorrected. ^{1}H- and ^{13}C NMR spectra were determined with Varian Unity Inova 200 and 500 MHz instruments (Varian, Palo Alto, CA, USA) in CD_3OD-d_6, $CDCl_3$ or DMSO-d_6, using tetramethylsilane (TMS) as the internal standard; chemical shifts are given in ppm values while coupling constants (*J*) are given in Hz. Signal multiplicities are characterized as s (singlet), d (doublet), t (triplet), q (quartet), m (multiplet), br (broad). Elemental analyses (C, H, N) were executed on a Carlo Erba Elemental Analyzer Mod. 1108 (Carlo Erba, Cornaredo, Italy); results were within ±0.4 % of the theoretical values. The characterization compounds **3**–**6** resulted in data that match with those previously reported in literature.

2.2.1. Synthesis of methyl 2-(4-bromobutoxy)-5-iodobenzoate (4)

In a sealed Pyrex glass tube equipped with a stirring bar, methyl 2-hydroxy-5-iodobenzoate (7.19 mmol, 1 eq), 1,4-dibromobutane (28.79 mmol, 4 eq) and K_2CO_3 (28.76 mmol, 4 eq) were dissolved in 12 mL of acetone. The mixture was stirred under microwave irradiation for 45 min (150 psi, 150 W, 100 °C). The crude was filtered to remove the inorganic solid, and the reaction solvent were removed under vacuum. Afterwards, the crude was purified by flash chromatography with a mixture of cyclohexane:ethyl acetate (9:1 v/v) as eluent.

White solid (yield: 56 %): mp 58.3–59.3 °C; IR (KBr) cm^{-1}: 3097, 2946, 1690, 1587, 1483, 1431, 1394, 1308, 1237, 821; ^{1}H NMR (DMSO-d_6) δ 7.89 (d, $J = 2.2$ Hz, 1H, aromatic), 7.82 (dd, $J = 8.8$, 2.4 Hz, 1H aromatic), 6.99 (d, $J = 8.6$ Hz, 1H aromatic), 4.06 (t, $J = 6.0$ Hz, 2H, OCH_2), 3.78 (s, 3H, OCH_3), 3.61 (t, $J = 6.6$ Hz, 2H, CH_2Br), 2.03–1.79 (m, 4H, CH_2CH_2).

2.2.2. Synthesis of methyl 2-(4-(1H-imidazol-1-yl)butoxy)-5-iodobenzoate (5)

In a sealed Pyrex glass tube equipped with a stirring bar, methyl 2-(4-bromobutoxy)-5-iodobenzoate (3.96 mmol, 1 eq), imidazole (5.94 mmol, 1.5 eq), and TBAB (catalytic, 0.1 eq) were dissolved in 9 mL of CH_3CN. The mixture was stirred under microwave irradiation for 45 min (150 psi, 150 W, 100 °C). Then, the mixture was diluted with 100 mL of

EtOAc, washed three times with NaOH 1 M (3×100 mL), dried with Na_2SO_4, filtered, and the solvent was removed under pressure.

The pale-yellow oil thus obtained was used in the next step without any further purification.

2.2.3. Synthesis of 2-(4-1H-imidazol-1-yl)butoxy)-5-iodobenzoic acid (6)

In a sealed Pyrex glass tube equipped with a stirring bar, the methyl 2-(4-(1*H*-imidazol-1-yl)butoxy)-5-iodobenzoate was dissolved in a mixture of THF:H_2O:CH_3OH (3:1.5:1 v/v ratio). LiOH (2 eq) was added, and the mixture was stirred under microwave irradiation for 45 min (150 psi, 150 W, 100 °C). Reaction solvents were removed under reduced pressure, and the residue was acidified till the isoelectric point is reached by dropwise addition of HCl 1 N. The aqueous phase was extracted with EtOAc (3×40 mL) in a separating funnel and the water phase was discarded. The funnel was then washed with MeOH. The two organic phases were dried with Na_2SO_4, filtered, and evaporated under vacuum, obtaining a white pure solid.

White solid (yield: 84 %): mp 89.5–90.5 °C; IR (KBr) cm^{-1}: 3386, 3132, 2939, 1590, 1465, 1400, 1242, 1104, 814, 748, 678, 633; ^{1}H NMR (200 MHz, CD_3OD) δ 8.64 (s, 1H, imidazole), 7.75 (d, J = 2.2 Hz, 1H aromatic), 7.64–7.54 (m, 2H, aromatic + imidazole), 7.35 (s, 1H, imidazole), 6.83 (d, J = 8.8 Hz, 1H, aromatic), 4.33 (t, J = 7.2 Hz, 2H. CH_2-imidazole), 4.06 (t, J = 5.6 Hz, 2H, OCH_2), 2.10 (m, J = 7.0 Hz, 2H, OCH_2CH_2), 1.87–1.70 (m, 2H, CH_2CH_2-imidazole).

2.2.4. General procedure for the synthesis of substituted 2-(4-(1H-imidazol-1-yl)butoxy)-5-iodobenzamides (7a-f)

In a round bottom flask, the 2-(4-1*H*-imidazol-1-yl)butoxy)-5-iodobenzoic acid (1 eq) was dissolved in 3 mL of anhydrous DMF under an argon atmosphere. The solution was cooled with ice to 0 °C. EDC hydrochloride (1.5 eq), HOBt (1.5 eq) and the appropriate amine (2 eq) were subsequently added to the cooled stirred solution, within 30 min, the pale-yellow resulting solution was left under stirring at room temperature for 24 h under argon atmosphere. Then the reaction solvent was concentrated under reduced pressure, the residue was diluted with 80 mL of a $NaHCO_3$ saturated solution, and the aqueous phase was extracted three times with EtOAc (3×40 mL). The organic phase was dried with Na_2SO_4, filtered, and evaporated under vacuum.

The crude was purified by flash chromatography by eluting with CH_2Cl_2:CH_3OH gradient mixtures. According to this procedure, the following products were obtained:

2.2.5. 2-(4-(1H-imidazol-1-yl)butoxy)-5-iodo-N-phenylbenzamide (7a)

This compound was obtained using 0.393 mmol of 2-(4-1*H*-imidazol-1-yl)butoxy)-5-iodobenzoic acid (**6**), 0.589 mmol of EDC hydrochloride, 0.589 mmol of HOBt and 0.786 mmol of aniline (a).

White solid (yield: 39 %) mp 68.2–70.2 °C; IR (KBr) cm^{-1} 3350, 2948, 2878, 1666, 1599, 1547, 1491, 1443, 1319, 1271, 1220, 1151, 1074, 1046, 906, 808, 753, 690, 664, 639, 536, 509; ^{1}H NMR (500 MHz, DMSO–d_6) δ 10.13 (s, 1H CONH), 7.84 (d, J = 2.0 Hz, 1H, aromatic), 7.78 (dd, J = 2.0, 9.0 Hz, 1H, aromatic), 7.66 (d, J = 8.0 Hz, 2H, aromatic), 7.53 (s, 1H, imidazole), 7.33 (t, J = 7.5 Hz, 2H, aromatic), 7.10 (t, J = 7.5 Hz, 1H, aromatic), 7.03 (s, 1H, imidazole), 7.00 (d, J = 9.0 Hz, 1H, aromatic), 6.83 (s, 1H, imidazole), 4.09 (t, J = 6.0 Hz, 2H, CH_2-imidazole), 3.96 (t, J = 7.0 Hz, 2H, OCH_2), 1.86–1.81 (m, 2H, OCH_2CH_2), 1.70–1.64 (m, 2H, CH_2CH_2-imidazole) (Fig. S1). ^{13}C NMR (125 MHz, DMSO–d6): δ 163.06, 155.62, 140.02, 138.80, 137.35, 128.82, 128.31, 128.15, 127.86, 126.74, 123.69, 119.47, 119.07, 115.73, 82.94, 67.99, 45.51, 27.20, 25.49 (Fig. S2). Anal. Calcd. For $C_{20}H_{20}IN_3O_2$: C, 52.07; H, 4.37; N, 9.11; O, 6.94. Found: C, 52.05; H, 4.37; N, 9.10; O, 6.95.

2.2.6. 2-(4-(1H-imidazol-1-yl)butoxy)-N-benzyl-5-iodobenzamide (7b)

This compound was obtained using 0.142 mmol of 2-(4-1*H*-imidazol-1-yl)butoxy)-5-iodobenzoic acid (**6**), 0.213 mmol of EDC hydrochloride, 0.213 mmol of HOBt and 0.284 mmol of benzylamine (b).

White solid (yield: 71 %) mp 63.5–65.5 °C; IR (KBr) cm^{-1} 3391, 2951, 1651, 1584, 1543, 1512, 1468, 1448, 1298, 1276, 1230, 1110, 1046, 814, 745; ^{1}H NMR (500 MHz, CD_3OD) δ 8.08 (d, J = 2.5 Hz, 1H, aromatic), 7.74 (dd, J = 2.5, 9 Hz, 1H aromatic), 7.32 (m, 5H, aromatic + imidazole), 7.00 (s, 1H, imidazole), 6.94 (s, 1H, imidazole), 6.91 (d, J = 9 Hz, 1H, aromatic), 4.56 (s, 2H, PhCH_2), 4.08 (t, J = 6.0 Hz, 2H, CH_2-imidazole), 3.90 (t, J = 7.0 Hz, 2H, OCH_2), 1.84–1.73 (m, 2H, OCH_2CH_2), 1.73–1.63 (m, 2H, CH_2CH_2-imidazole) (Fig. S3). ^{13}C NMR (125 MHz, CD_3OD): 166.84, 157.90, 142.35, 140.14, 139.67, 129.74, 129.03, 128.77, 128.53, 128.25, 120.41, 116.36, 83.43, 69.75, 47.49, 44.65, 28.67, 27.04 (Fig. S4). Anal. Calcd. For $C_{21}H_{22}IN_3O_2$: C, 53.06; H, 4.67; N, 8.84; O, 6.73. Found C, 53.08; H, 4.67; N, 8.83; O, 6.74.

2.2.7. 2-(4-(1H-imidazol-1-yl)butoxy)-N-(adamantan-1-yl)-5-iodobenzamide (7c)

This compound was obtained using 0.349 mmol of 2-(4-1*H*-imidazol-1-yl)butoxy)-5-iodobenzoic acid (**6**), 0.523 mmol of EDC hydrochloride, 0.523 mmol of HOBt and 0.698 mmol of adamantylamine (c).

White solid (yield: 32 %) mp 89.6–91.6 °C; IR (KBr) cm^{-1} 3384, 2907, 2847, 1658, 1583, 1538, 1464, 1388, 1358, 1301, 1271, 2229, 1084, 812, 732, 664, 529; ^{1}H NMR (500 MHz, DMSO-d_6) δ 7.89 (d, J = 2.5 Hz, CONH), 7.73–7.70 (m, 2H, aromatic), 7.61 (s, 1H, imidazole), 7.15 (s, 1H, imidazole), 6.93 (d, J = 9 Hz, 1H, aromatic), 6.87 (s, 1H, imidazole), 4.05 (dt, J = 14.1, 6.7 Hz, 4H, OCH_2 + CH_2-imidazole), 2.03 (s, 3H, adamantane), 1.96 (d, J = 2.5 Hz, 6H, adamantane), 1.91–1.83 (m, 2H, OCH_2CH_2), 1.73–1.66 (m, 2H, CH_2CH_2-imidazole), 1.66–1.60 (m, 6H, adamantane) (Fig. S5). ^{13}C NMR (125 MHz, DMSO-d_6): 162.41, 155.87, 139.95, 138.10, 137.17, 128.33, 126.55, 119.19, 115.79, 83.25, 68.26, 51.37, 45.54, 41.01, 35.98, 28.83, 27.35, 25.72 (Fig. S6). Anal. Calcd. For $C_{24}H_{30}IN_3O_2$: C, 55.50; H, 5.82; N, 8.09; O, 6.16. Found C, 55.52; H, 5.82; N, 8.08; O, 6.15.

2.2.8. 2-(4-(1H-imidazol-1-yl)butoxy)-N-benzhydryl-5-iodobenzamide (7d)

This compound was obtained using 0.401 mmol of 2-(4-1*H*-imidazol-1-yl)butoxy)-5-iodobenzoic acid (**6**), 0.601 mmol of EDC hydrochloride, 0.601 mmol of HOBt and 0.802 mmol of dyphenylmethanamine (d). Sticky oil (yield: 32 %), IR (NaCl) cm^{-1} 3391, 2942, 1653, 1586, 1522, 1464, 1389, 1273, 1229, 1110, 1078, 1029, 907, 811, 741, 700; ^{1}H NMR (500 MHz, CD_3OD) δ 8.10 (d, J = 2.5 Hz, 1H, aromatic), 7.74 (t, J = 8 Hz, 1H, aromatic), 7.52 (s, 1H, imidazole), 7.36–7.24 (m, 10*H* aromatic + 1H, imidazole), 6.97 (s, 1H, imidazole), 6.95–6.88 (m, 2H, aromatic), 6.32 (s, 1H, C*H*NH), 4.11–4.04 (m, 2H, CH_2-imidazole), 3.86–3.80 (m, 2H, OCH_2), 1.73–1.65 (m, 2H, CH_2CH_2-imidazole), 1.62 (m, 2H, OCH_2CH_2) (Fig. S7). ^{13}C NMR (125 MHz, CD_3OD): 166.24, 158.56, 143.35, 143.13, 140.88, 130.30, 129.53, 129.49, 129.14, 129.02, 125.95, 120.92, 116.88, 84.17, 70.42, 59.58, 47.92, 29.05, 27.58 (Fig. S8). Anal. Calcd. For $C_{27}H_{26}IN_3O_2$: C, 58.81; H, 4.75; N, 7.62; O, 5.80. Found C, 58.83; H, 4.74; N, 7.61; O, 5.79.

2.2.9. 2-(4-(1H-imidazol-1-yl)butoxy)-N-(3-benzylphenyl)-5-iodobenzamide (7e)

This compound was obtained using 0.137 mmol of 2-(4-1*H*-imidazol-1-yl)butoxy)-5-iodobenzoic acid (**6**), 0.206 mmol of EDC hydrochloride, 0.206 mmol of HOBt and 0.274 mmol of 3-benzylaniline (e).

White solid (yield: 56 %) mp 149–151 °C; IR (KBr) cm^{-1} 3351, 2941, 1665, 1598, 1584, 1543, 1493, 1468, 1442, 1317, 1223, 1172, 1074, 1003, 809, 832, 753, 691, 662, 637, 534, 506. ^{1}H NMR (500 MHz, DMSO-d_6) 10.09 (s, 1H, aromatic), 7.81 (d, J = 2.5 Hz, 1H, aromatic), 7.76 (dd, J = 2.5, 9 Hz, 1H, aromatic), 7.56 (s, 1H, aromatic), 7.53 (s, 1H, imidazole), 7.48 (d, J = 8.5 Hz, 1H, aromatic), 7.32–7.16 (m, 6H, aromatic), 7.01 (s, 1H. imidazole), 6.98 (m, 2H, aromatic), 6.82 (s, 1H, imidazole), 4.06 (t, J = 6 Hz, 2H, PhCH_2Ph), 3.96–3.89 (m, 4H, OCH_2 + CH_2-imidazole), 1.85–1.76 (m, 2H, OCH_2CH_2), 1.64 (m, 2H, CH_2CH_2-imidazole) (Fig. S9). ^{13}C NMR (125 MHz, DMSO-d_6): 163.00, 155.58, 141.90, 141.05, 139.94, 138.92, 137.31, 137.10, 130.02, 128.83,

128.68, 128.40, 128.31, 127.90, 125.98, 124.13, 119.70, 119.03, 117.23, 115.68, 82.90, 67.91, 45.44, 41.19, 27.13, 25.40 (Fig. S10). Anal. Calcd. For $C_{27}H_{26}IN_3O_2$: C, 58.81; H, 4.75; N, 7.62; O, 5.80 Found C, 58.79; H, 4.74; N, 7.63; O, 5.81.

2.2.10. 2-(4-(1H-imidazol-1-yl)butoxy)-N-(4-chlorobenzyl)-5-iodobenzamide (7f)

This compound was obtained using 0.349 mmol of 2-(4-1*H*-imidazol-1-yl)butoxy)-5-iodobenzoic acid (**6**), 0.183 mmol of EDC hydrochloride, 0.183 mmol of HOBt and 0.244 mmol of 4-Chlorobenzylamine (f).

White solid (yield: 75 %) mp 64.3–66.4 °C; IR (KBr) cm^{-1} 3395, 2953, 1652, 1583, 1543, 1511, 1469, 1443, 1292, 1275, 1232, 1111, 1048, 814, 746, 623, 523, 478. ^{1}H NMR (500 MHz, CD_3OD) δ 8.08 (d, J = 2.5 Hz, 1H, CONH), 7.78 (dd, J = 2.5, 8.5 Hz, 1H, aromatic), 7.63 (s, 1H, imidazole), 7.40–7.30 (m, 5H, aromatic), 7.08 (s, 1H, imidazole), 6.99 (s, 1H, imidazole), 6.95 (d, J = 8.5 Hz, 1H, aromatic), 4.58 (s, 2H, PhCH_2), 4.12 (t, J = 6.5 Hz, 2H, OCH_2), 3.99 (t, J = 7.0 Hz, 2H, CH_2-imidazole), 1.84 (m, 2H, OCH_2CH_2), 1.80–1.69 (m, 2H, CH_2CH_2-imidazole) (Fig. S11). ^{13}C NMR (125 MHz, CD3OD): 167.15, 157.92, 142.42, 140.12, 138.78, 134.26, 130.48, 130.32, 129.85, 129.73, 129.24, 126.55, 116.47, 83.49, 69.80, 47.62, 43.97, 28.82, 27.14 (Fig. S12). Anal. Calcd. For $C_{21}H_{21}ClIN_3O_2$: C, 49.48; H, 4.15; N, 8.24; O, 6.28 Found C, 49.45; H, 4.16; N, 8.23; O, 6.31.

2.2.11. General procedure for the synthesis of substituted 4-(4-(1H-imidazol-1-yl)butoxy)-[1,1′-biphenyl]-3-carboxamides (8a-c)

In a previously dried Pyrex glass tube, the proper substituted 4-(4-(1*H*-imidazol-1-yl)butoxy)-[1,1′-biphenyl]-3-carboxamide (**8a-c**) (1 eq) was dissolved in 3 mL of degassed toluene, under an argon atmosphere. Phenylboronic acid (2.2 eq), tetrakis(triphenylphospine)palladium(0) (0.1 eq) and K_3PO_4 (4 eq) were added to the solution as enumerated.

The mixture was reacted under microwave irradiation for 15 min (6 psi, 55 W, 121 °C). The reaction mixture was diluted in CH_2Cl_2 and washed three times with $NaHCO_3$ 5 % (3×100 mL), dried using Na_2SO_4, filtered, and evaporated under vacuum. The crude was purified by flash chromatography eluting with gradient mixtures of CH_2Cl_2:CH_3OH. According to this procedure, the following products were obtained:

2.2.12. 4-(4-(1H-imidazol-1-yl)butoxy)-N-phenyl-[1,1′-biphenyl]-3-carboxamide (8a)

This compound was obtained using 0.0438 mmol of 2-(4-(1*H*-imidazol-1-yl)butoxy)-5-iodo-N-phenylbenzamide (**7a**), 0.0963 mmol of phenylboronic acid, catalytic amount of tetrakis(triphenylphospine) palladium(0), and 0.175 mmol of K_3PO_4.

White solid (yield: 82 %) mp 76.5–78.5 °C; IR (KBr) cm^{-1} 3353, 3064, 2947, 1662, 1600, 1538, 1499, 1442, 1404, 1319, 1275, 1110, 1075, 1021, 907, 811, 755, 707, 576, 535, 508; ^{1}H NMR (500 MHz, $CDCl_3$) δ 9.43 (s, 1H, CONH), 8.45 (d, J = 2.0 Hz, 1H, aromatic), 8.04–7.99 (m, 2H, aromatic), 7.80 (s, 1H, imidazole), 7.69 (dd, J = 2.0, 8.5 Hz, 1H, aromatic), 7.55 (d, J = 8.0 Hz, 2H aromatic), 7.39–7.32 (m, 3H + 1H, aromatic + imidazole), 7.26 (s, 1H, aromatic), 7.13 (m, 2H, aromatic), 6.81 (s, 1H, imidazole), 6.69 (d, J = 9 Hz, 1H, aromatic), 4.12 (t, J = 6.5 Hz, 2H, OCH_2), 4.02 (t, J = 7.0 Hz, 2H, CH_2-imidazole), 1.99 (m, 2H, CH_2CH_2-imidazole), 1.90 (m, 2H, OCH_2CH_2) (Fig. S13). ^{13}C NMR (125 MHz, DMSO-d_6): 163.1, 155.57, 139.99, 138.81, 137.31, 134.05, 130.01, 128.81, 127.98, 127.35, 123.68, 119.44, 115.74, 82.98, 67.91, 46.37, 26.90, 25.36 (Fig. S14). Anal. Calcd. For $C_{26}H_{25}N_3O_2$: C, 75.89; H, 6.12; N, 10.21; O, 7.78. Found C, 75.87; H, 6.11; N, 10.22; O, 7.80.

2.2.13. 4-(4-(1H-imidazol-1-yl)butoxy)-N-benzyl-[1,1′-biphenyl]-3-carboxamide (8b)

This compound was obtained using 0.042 mmol of 2-(4-(1*H*-imidazol-1-yl)butoxy)-N-benzyl-5-iodobenzamide (**7b**), 0.092 mmol of phenylboronic acid, catalytic amount of tetrakis(triphenylphospine) palladium(0), and 0.168 mmol of K_3PO_4.

White solid (yield: 85 %) mp 73.8–75.8 °C; IR (KBr) cm^{-1} 3391, 2950, 1644, 1585, 1538, 1443, 1404, 1275, 1230, 1110, 1082, 908, 814, 745, 702, 664, 603, 534, 488; ^{1}H NMR (500 MHz, $CDCl_3$) δ 8.47 (d, J = 2.0 Hz, 1H, aromatic), 8.03 (d, J = 3.5 Hz, 1H, aromatic), 7.86 (s, 1H, aromatic), 7.80 (s, 1H, imidazole), 7.67 (d d, 1H, aromatic), 7.40–7.27 (m, 7H, aromatic), 7.26 (s, 1H, aromatic), 7.15 (s, 1H, imidazole), 6.75 (s, 1H, imidazole), 6.65 (t, J = 7.5 Hz, 1H, aromatic), 4.62 (t, J = 6.0 Hz, 2H, CH_2NHCO), 4.05–3.95 (m, 4H, CH_2-imidazole), 3.71 (m, 2H, OCH_2), 1.75–1.55 (m, 4H, $OCH_2CH_2CH_2$-imidazole) (Fig. S15). ^{13}C NMR (125 MHz, DMSO-d_6): 164.20, 155.83, 140.00, 139.13, 137.89, 137.79, 134.07, 130.04, 128.39, 128.31, 127.38, 127.20, 126.87, 126.72, 120.50, 115.77, 83.07, 68.01, 46.75, 42.67, 26.68, 25.18 (Fig. S16). Anal. Calcd. For $C_{27}H_{27}N_3O_2$: C, 75.89; H, 6.12; N, 10.21; O, 7.78. Found C, 75.91; H, 6.11; N, 10.20; O, 7.77.

2.2.14. 4-(4-(1H-imidazol-1-yl)butoxy)-N-(adamantan-1-yl)-[1,1′-biphenyl]-3-carboxamide (8c)

This compound was obtained using 0.063 mmol of 2-(4-(1*H*-imidazol-1-yl)butoxy)-N-(adamantan-1-yl)-5-iodobenzamide (**7c**), 0.138 mmol of phenylboronic acid, catalytic amount of tetrakis(triphenylphospine)palladium(0), and 0.252 mmol of K_3PO_4.

White/transparent solid (yield: 77 %) mp 85.8–87.8 °C; IR (KBr) cm^{-1} 3384, 2906, 2848, 1652, 1540, 1443, 1404, 1301, 1276, 1250, 1102, 1084, 1021, 813, 746, 707; ^{1}H NMR (500 MHz $CDCl_3$) δ 8.32 (d, J = 2.0 Hz, 1H, CONH), 8.08 (s, 1H, imidazole), 8.02 (s, 2H, aromatic), 7.63 (dd, J = 2.0, 8.5 Hz, 1H, aromatic), 7.37 (m, 3H, aromatic), 7.26 (d, J = 4.0 Hz, 2H, aromatic), 7.24 (s, 1H, imidazole), 6.97 (s, 1H, imidazole), 6.63 (d, J = 9 Hz, 1H, aromatic), 4.08 (dt, J = 7.5 Hz,14.5 Hz, 4H, OCH_2 + CH_2-imidazole), 2.22–1.97 (m, 9H + 2H adamantane + OCH_2CH_2), 1.86 (m, 2H, CH_2CH_2-imidazole), 1.71 (d, J = 8.5 Hz, 6H, adamantane) (Fig. S17). ^{13}C NMR (125 MHz, $CDCl_3$): 162.64, 155.83, 140.70, 140.64, 140.57, 140.15, 133.58, 127.81, 127.41, 125.75, 114.66, 114.44, 84.04, 68.38, 68.16, 52.22, 47.98, 41.81, 36.41, 36.38, 29.45, 29.42, 27.42, 27.26, 26.31, 26.04 (Fig. S18). Anal. Calcd. For $C_{30}H_{35}N_3O_2$: C, 76.73; H, 7.51; N, 8.95; O, 6.81. Found C, 76.75; H, 7.50; N, 8.96; O, 6.79.

2.3. Inhibitory activity test on heme oxygenase

2.3.1. Preparation of rat spleen microsomal fractions

HO-1 and HO-2 are proteins abundant in rat spleen and brain, respectively (Vlahakis et al., 2012), and therefore, were obtained as the microsomal fraction of these tissues by differential centrifugation according to the protocol previously described by Ryter et al., 2006. This particular microsomal preparation was selected to use the most native HO-1 and HO-2 form (i.e., closest to *in vivo*). The present experiments complied with current Italian law and met the guidelines of the Institutional Animal Care and Use Committee of the Ministry of Health (Directorate General for Animal Health and Veterinary Medicines, Italy) "Dosing of enzymatic activities in rat microsomes: evaluation of the effect of natural and synthetic molecules" (2023–2025), project code 1984F.N.FGE. Male Sprague–Dawley albino rats (150 g body weight and 45 days age), kept at room temperature with a natural photoperiod (12 h light-12 h dark cycle) and free access to water, were used to obtain spleen and brain microsomal fraction. Each rat was sacrificed, and their spleens and brains were resected and weighed. A homogenate (15 %, w/v) of spleens or brain from five rats was prepared in 50 mM Tris buffer, pH 7.4, containing 0.25 M sucrose, using a Potter-Elvehjem tissue grinder with a Teflon pestle. Then, the microsomal fraction was obtained by differential centrifugation (Optima TLX ultracentrifuge, Beckman Coulter, Indianapolis, IN, USA) from the formed homogenate: a first centrifugation at 10,000g for 20 min at 4 °C, followed by the second centrifugation of the supernatant at 100,000g for 60 min at 4 °C. The obtained microsomes pellet was then resuspended in 100 mM potassium phosphate buffer, pH 7.8, containing 2 mM $MgCl_2$. Finally, the obtained microsomal fraction of rat spleen and brain were divided in equal

aliquots and placed into microcentrifuge tubes, which were stored at −80 °C for up to 2 months before use.

2.3.2. Preparation of biliverdin reductase

Biliverdin reductase was obtained by using rat liver cytosol. Three volumes of a 1.15 % KCl w/v and Tris buffer 20 mM solution (pH 7.8) was used to homogenize the liver tissue, on ice. Homogenates were centrifuged at 10,000g for 20 min at 4 °C, and the obtained supernatant was then centrifuged at 100,000g for 1 h at 4 °C to pellet the microsomes. After nanodrop protein quantification, the 100,000g supernatant was stored in small amounts at − 80 °C.

2.3.3. Measurement of HO-1 enzymatic activities in rat spleen

The HO-1 or HO-2 activity was determined by measuring the bilirubin formation quantifying the absorbance at 464–530 nm as described by Ryter et al., 2006. Incubation mixtures (500 μL) contained 20 mM Tris–HCl, pH 7.4, (1 mg/mL) microsomal extract, 0.5–2 mg/mL biliverdin reductase, 1 mM NADPH, 2 mM glucose 6-phosphate (G6P), 1 U G6P dehydrogenase, 25 μM hemin, and 10 μL of DMSO (or the same volume of DMSO containing the test compounds to a final concentration of 100, 10, and 1 μM).

Enzymatic reactions were carried out at 37 °C for 60 min in a circulating water bath in the dark, in triplicate. The addition of 500 μL of chloroform stopped the reactions. After recovering the chloroform phase, a double-beam spectrophotometer (Hitachi U-2000, Hitachi, Tokyo, Japan) was used to measure the amount of bilirubin formed quantifying OD at 464 and 530 nm (extinction coefficient 40 mM/cm^{-1}). The enzymatic activity was defined as Units (one Unit is the amount of enzyme catalysing the formation of 1 nmol of bilirubin/mg protein/h).

2.4. NCI-60 panel antitumoral screening

The NCI-60 panel testing details are available in the NCI website page at https://dtp.cancer.gov/discovery_development/nci-60/default.htm (accessed 15/09/24) (dtp.cancer.gov, n.d). Briefly, tumoral cell lines were seeded in 96-well plates at an appropriate density for 24 h. Some well plates were used to determine the initial cell density after 1 day of seeding (time zero), while the remaining well plates were incubated with a 10 μM concentration of the test compound for 48 h. After this period, cell monolayers were stained with sulphorodamine B and the net growth inhibition and cell killing capacity was calculated taking into consideration the number of control cells without drug treatment and the density at time zero (Holbeck et al., 2010).

2.5. NLC preparation and characterization

2.5.1. NLC preparation

Nanostructured lipid carriers were prepared by a high shear homogenization method (Rouco et al., 2020). Specifically, in a 50 mL falcon tube, 5 mg of compound 7b (VP21-04) was dissolved in 150 mg of Labrasol ALF. Successively, 150 mg of Compritol 888 ATO was added to the mixture. Meanwhile, in another tube, 1.5 mg of lecithin was dissolved in 10 mL of Tween 80 solution (1.8 % v/v in Double Distilled Water; DDW). Both tubes were heated at 85 °C for 5 min. After heating, the 10 mL of lecithin/Tween solution was added to the drug/lipid phase tube, and the mixture was homogenized at 14,600 rpm and 85 °C for 10 min using an Ultra-Turrax T25 (IKA Labortechnik, Staufen, Germany). Then, the NLC dispersion was immediately placed on an ice bath for 2 min and stored in fridge for 1 h. Successively, the dispersion was filtered with a 0.22 μm filter in sterility condition and stored at 4 °C until use (hereafter called NLC 21–04). Blank nanoparticles, without VP21-04, were also prepared using the same procedure (hereafter called Blank NLC).

2.5.2. Size, PDI and Z. Pot analysis of NLC

A Malvern Zetasizer Pro (Malvern Panalytical, United Kingdom) was used to analyze the size, polydispersity index (PDI), and Zeta potential of the NLC 21–04 and Blank NLC. The nanoparticle dispersions were diluted in DDW until reaching appropriate concentration for the analysis. All tests were conducted in triplicate. The same method was used to assess the NPs stability, to this end, the initial dispersions were split in three parts and stored at 4 °C, room temperature (r.t), and 37 °C and analyzed at prefixed timepoints (0, 2, 4, 7, 14, 21, and 30 days).

2.5.3. Drug loading

To calculate the drug loading and encapsulation efficiency, 100 μL of each nanoparticle dispersion was added to 900 μL of acetonitrile (ACN) and vortexed for 1 min to allow nanoparticle system rupture and drug release. Thus, the solution was centrifuged at 14,000 rpm for 15 min at r.t. to separate the lipid pellet from the drug solution supernatant. The same procedure was also conducted on Blank NLC.

Successively, the supernatant was analyzed by means of an Agilent 8453 UV–vis spectrophotometer (Agilent, Waldbronn, Germany), the drug concentration was determined at 300 nm using a calibration curve of the free-drug in ACN using the Blank NLC supernatants as zero. The drug loading was calculated using Equation (1), while Equation (2) was used to calculate the encapsulation efficiency (E.E.). The results are reported as the mean of tests conducted in triplicate:

$$Drug\ loading\% = \frac{weight\ of\ drug}{total\ weight\ nanoparticles} \times 100 \quad (1)$$

Where the *weight of drug* is the amount of encapsulated drug determined by UV–vis spectroscopy, and *tot weight nanoparticles* is the weight of the materials used to obtain the nanoparticles.

$$E.E.\% = \frac{weight\ of\ drug}{init.\ drug\ weight} \times 100 \quad (2)$$

Where the *weight of drug* is the amount of encapsulated drug determined by UV–vis spectroscopy and *init. drug weight* is the initial amount of drug used for formulation.

2.5.4. UV–vis absorbance profile analysis

The UV–vis absorption profile of the free-drug, blank, and loaded nanoparticles was analyzed using an Agilent 8453 UV–vis spectrophotometer (Agilent, Waldbronn, Germany). The drug was dissolved in ACN and diluted in ACN until reaching the following concentrations: 50 μg/mL, and 25 μg/μL. The Blank NLC and NLC 21–04 were diluted in DDW to reach a concentration of 50 μL/mL, that led to adequate absorbance values. Moreover, 100 μL of NLC 21–04 were added to 900 μL of ACN, vortexed, and centrifuged as reported in section 2.5.3. to allow the complete release of the encapsulated drug. The absorption profile of the abovementioned solutions was analyzed from 190 nm to 800 nm.

For the UV–vis stability study of the NLC 21–04 nanoparticle systems, a dilution of the system was done in DDW reaching concentration of 50 μL/mL. The solution was stored at 4 °C, r.t, and 37 °C for 7 days and the absorption spectra was analyzed at prefixed timepoints (0, 4, and 7 days).

2.5.5. TEM analysis

Nanoparticles morphology, structure, and size were analyzed by transmission electron microscopy (TEM). To prepare the sample for the analysis, 10 μL of each sample were placed on a cooper grid covered by a carbon membrane. Successively, the samples were stained with phosphotungstic acidic solution (2 % w/v) for 2 min, and finally analyzed at 120 kV by means of a JOEL microscope (JEM 2010, Japan). Images were acquired using a Gatan Orius camera (Gatan inc, Pleasanton, CA, USA).

2.6. In vitro antitumoral testing and cytocompatibility

2.6.1. Cell culture treatments

Two cancer cell lines of metastatic breast cancer (MDA-MB-468) and melanoma (SK-MEL-5) were selected to analyze the antitumoral activity based on the NCI-60 panel antitumoral screening. Both cell lines were obtained from the American Type Culture Collection (ATCC, Rockville, MD). MDA-MB-468 cells were grown in DMEM supplemented with 10 % of heat-inactivated FBS and 1 % of anti-anti, while the SK-MEL-5 were grown in EMEM supplemented with 10 % of heat-inactivated FBS and 1 % of anti-anti. BALB/3T3, also obtained from ATCC, were cultured in DMEM supplemented with 10 % of heat-inactivated FBS and 1 % of anti-anti. Cells were incubated at 37 °C in a humidified atmosphere with 5 % CO_2 changing media every other day and splitting the cells when reaching 80 % confluency.

2.6.2. Cell viability assay

The effect of compound **7b** (VP 21–04), Blank NLC, and NLC 21–04 on MD-MB-468, SK-MEL-5 and BALB/3T3 cell viability was assessed by performing an Alamar blue cell viability assay. Cells were seeded into 96-well plates at a 10×10^3 cells/well density in 150 μL of culture medium and let them attach for 24 h. After 24 h, cells were treated with the test samples at four different drug equivalent concentrations (5, 10, 25, and 50 μM) for 24 h and 48 h. DMSO 0.1 % v/v in cell culture media solution was used as control for the drug treatment, while pure culture media was used as control for the nanoparticle systems. After the treatments, 150 μL of a 9 % Alamar blue (Sigma-Aldrich) was added to each well and incubated for 2 h at 37 °C. Finally, fluorescence was measured at 580 nm using excitation at 540 nm in a FLUOstar Optima microplate reader (BMG Labtech, Ortenberg, Germany). Five replicate wells were used for each group and experiment, results are expressed as the median of three independent experiments.

2.7. In ovo antitumoral test

The chorioallantoic membrane (CAM) tumor grafted model was used as an alternative to other *in vivo* tests to study the antitumoral activity of the NLC 21–04 towards metastatic breast cancer (MDA-MB-468).

Fertilized hen eggs (Coren, San Cibrao das Viñas, Spain) were incubated at 37 °C and 60 % relative humidity (RH) and rotated periodically. On day 3, 2 mL of albumin was removed from the acute pole of the eggs, and the presence of the embryo was checked by opening a small window of 1 cm × 1 cm. The opened windows were then covered with films to prevent contamination and drying out, and the eggs were incubated in horizontal position. On day 7 incubation, before grafting, MDA-MD-468 cells were labelled with 10 μM CellTracker™ Green CMFDA for 45 min. Then, cells were washed with DPBS to remove excess of cell tracker, trypsinized, centrifuged, and resuspended in culture media for counting using a Coulter Counter (Multisizer 3, Beckman Coulter, Brea, CA, USA). Afterwards, cells were centrifuged again, and the pellet was resuspended in adequate amount of DPBS to achieve the desired concentration. The cell suspension (20 μL; $2.5\cdot10^6$ cells) was mixed with 40 μL of Corning™ Matrigel™ and 10 μL of the treatment solution. Five treatment groups were included: 25 μM or 10 μM final concentration of NLC 21–04 dispersion in DPBS; 25 μM or 10 μM final concentration of Blank NPs in DPBS; or DPBS (control). Each condition was tested in triplicate. The window of the eggs was further opened to accommodate a sterilized polycaprolactone (PCL) ring (Ø 1 cm) over the CAM, which identified the region of grafting. Thus, the obtained mixtures were pipetted into the rings and eggs were kept for 30 min at r.t. to allow Matrigel gelation. Successively, the window was re-covered with new film, and the eggs were returned to the incubator until day 10. All the eggs manipulation procedure was conducted maintaining sterile conditions and protecting the labelled cells from light. After the incubation period, the eggs were withdrawn from the incubator and the window was further enlarged to allow macroscopical visualization analysis. Then, images of the tumor grafted CAM were acquired using a Leica MZ16F fluorescence stereomicroscope (Leica, Wetzlar, Germany) both in brightfield and in fluorescence mode, to visualize the tumor growth. The mean and maximum intensity of fluorescence was calculated using ImageJ software (National Institutes of Health, MD, USA), randomly placing a circular region of interest (ROI) with a diameter of 135 pixel on three different spots of the tumor. The vasculature formation around the solid tumor was evaluated through macroscopical visual analysis counting the number of vessels. All calculations were performed in triplicate.

2.8. Statistical analysis

Statistical analyses were performed using GraphPad Prism software (GraphPad software, La Jolla, CA, USA). The one-way analysis of variance (ANOVA) and Tukey's multiple comparison post-tests were performed, considering significant differences for $p < 0.05$. 0.1234 (ns), 0.0332 (*), 0.0021 (**), 0.0002 (***), <0.0001 (****).

3. Results and discussion

3.1. Rational design of the inhibitors

In the present work newly HO-1 inhibitors were designed based on our previously synthesized compounds (compound **1** and **2a,b**) that showed inhibitory potency towards HO-1 (Fig. 1) (Floresta et al., 2021b; Salerno et al., 2013). Unfortunately, on these compounds a potent inhibition was also achieved on HO-2, lacking on selectivity between the two isoforms. Both isoforms share ~76 % similar aminoacidic sequence, and the mechanism of non-competitive inhibitions is shared. Indeed, as evidenced by crystallographic and structure activity relationship data, the HO family counts with three main crucial regions for the non-competitive inhibition. For Azalanstat-like small compounds derivatives, the coordination of the heme ferrous ion by azole rings (e.g. imidazole, triazole) represents the anchor point with the enzyme, blocking the heme catabolism (Amata et al., 2017b; Vlahakis et al., 2005). The region where heme allocates is commonly called eastern region, which is 34 $Å^3$ larger in HO-2 than HO-1. The binding site presents other two hydrophobic regions: the north-western (smaller) and western (bigger), located in the near and distal area. Both regions are able to establish hydrophobic interactions with the inhibitors, further stabilizing the binding poses and being responsible for potency and selectivity (Fig. S19) (Rahman et al., 2013). The analysis of five different HO-1/ligand co-crystals (PDB ID: 3CZY, 3HOK, 3TGM, 3K4F and 2DY5) showed a certain flexibility of the binding cavity, which can be adapted to the ligands (Rahman et al., 2013; Salerno et al., 2019). In co-crystal 3HOK, the compound QC-80 was able to cause a shifting in the proximal helix of HO-1 enzyme, thanks to a large and bulky northeastern substituent, inducing the formation of an additional secondary small hydrophobic pocket (Amata et al., 2017a; Rahman et al., 2012). Bearing this in mind, we hypothesize that the combination between the 4-iodophenoxybutylimidazolic moiety of compound **1** and the 2-oxybenzamide moiety of compounds **2a,b**, can offer an opportunity to finely tune the compound **1** structure to increase the selectivity for HO-1, while maintaining or ameliorating the potency (Fig. 1). Indeed, the substitution of the amide moiety with lipophilic groups of different bulkiness may allow to establish stronger interactions with the hydrophobic pockets, exploiting their flexibility to unveil novel chances for selectivity towards the two isoforms. Moreover, taking advantages of the high reactivity of the iodine group in position 5 of the central 2-oxybenzamide moiety, an additional phenyl group was added to some derivatives to also evaluate the effect of this modification on potency and selectivity towards HO-1 (Fig. 1).

3.2. Chemistry

The synthesis of the designed compounds followed the Scheme 1.

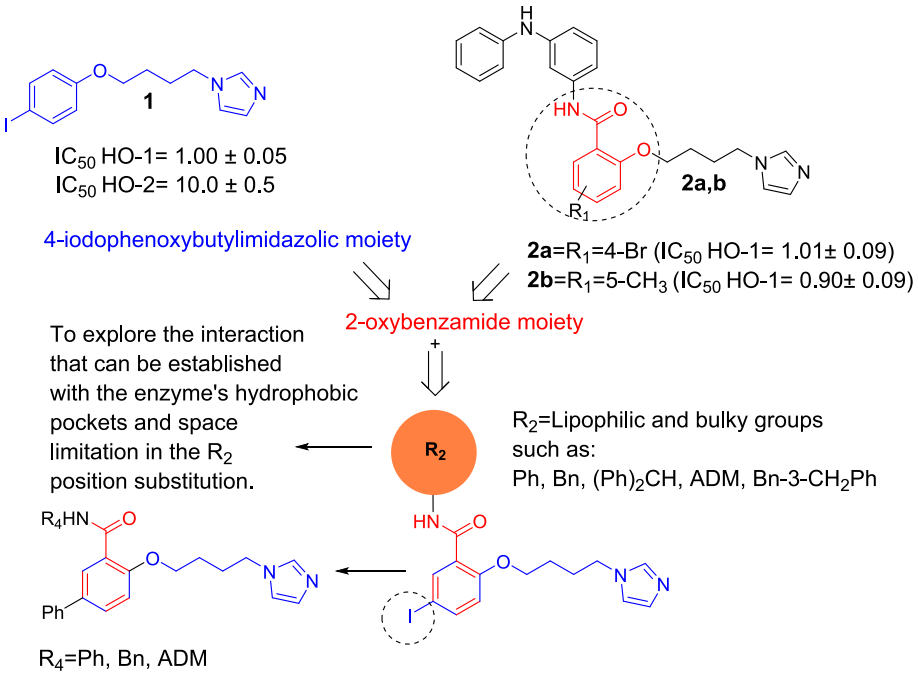

Fig. 1. Rational design of the newly synthesized HO-1 inhibitors.

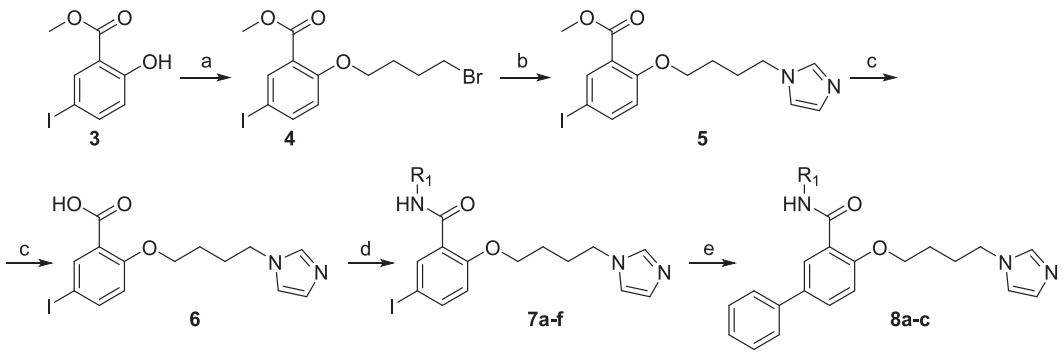

Compound	R1 *
7a	-Ph
7b (VP 21-04)	-Bn
7c	-ADM
7d	$(Ph)_2CH$-
7e	Bn-3-CH_2Ph-
7f	Cl-Bn-
8a	-Ph
8b	-Bn
8c	-ADM

Scheme 1. A) 1,4-dibromobutane, acetone, k_2CO_3, 90 °C, MW, 45 min; b) imidazole, CH_3CN, TEA, TBAB,

Briefly, starting from methyl 2-hydroxy-5-iodobenzoate (**3**) compound **4** was obtained by means of a nucleophilic substitution (SN) performed under Microwave Assisted Organic Synthesis (MAOS) conditions. Successively, the obtained bromine-derivate (**4**) was reacted with imidazole under MAOS conditions, to achieve compound **5**. The carboxylic acid derivate compound **6** was obtained starting from the imidazole-ester derivate **5**, hydrolyzed in MAOS conditions by LiOH. Then, the obtained carboxylic acid derivate **6** was subjected to an acyl nucleophilic substitution with the appropriate amine based on the desired final structure (**a-f**) in the presence of EDC hydrochloride and HOBt to obtain the final amide derivatives **7a-f**. The other series **8a-c** was obtained by means of a Suzuki–Miyaura coupling reaction, conducted in MAOS conditions, starting from compounds **7a-c.**

95 °C, MW, 45 min; c) LiOH, THF/H_2O/CH_3OH, MW, 150 psi, 150 W, 100 °C, 90 min; d) EDC hydrochloride, HOBt, appropriate amine (a-f), anhydrous DMF, 0 °C, then room temperature, 24 h, under Ar; e) Phenylboronic acid, $Pd(PPh_3)_4$, K_3PO_4, Toluene dry, MW, 6 psi, 55 W, 121 °C, 15 min, under Ar. *ADM: adamantane, Ph: Phenyl, Bn: Benzyl.

3.3. HO inhibitory activity

The enzyme inhibitory activity of the newly synthesized compounds **7a-f** and **8a-c** was measured using the spleen microsomal fraction, where HO-1 isoform is abundant. The inhibitory activity, expressed as the concentration of compound able to inhibit 50 % of the activity of the enzyme (IC_{50}), is reported in micromolar (μM). The obtained data are reported in Table 1.

The results showed that only compound **7b**, possessing a benzyl

Table 1
IC_{50} values of the novel HO-1 inhibitors **7a-f** and **8a-c** series.[a].

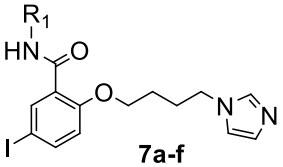

7a-f

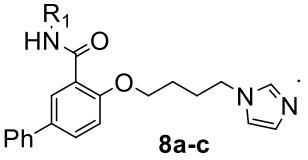

8a-c

Compound	R_1	IC_{50} HO-1 (μM)	IC_{50} HO-2 (μM)
7a	−Ph	61.78±0.16	N.T.
7b (VP 21–04)	−Bn	0.9±0.08	38±0.2
7c	−ADM*	50±1.63	N.T.
7d	$(Ph)_2CH$–	76.16±1.31	N.T.
7e	Bn-3-CH_2Ph-	106±0.6	N.T.
7f	Cl-Bn-	50.7±0.05	N.T.
8a	Ph-	78.34±1.76	N.T.
8b	Bn-	76.16±1.76	N.T.
8c	−ADM	83.79±0.61	N.T.

Values are the mean of triplicate experiments; N.T. = not tested. *ADM: adamantane, Ph: Phenyl, Bn: Benzyl.

[a] Data are shown as IC_{50} values in μM ± standard deviation (SD).

moiety and an iodine at the 5-position of the central aryl group, gave an IC_{50} value towards HO-1 in the very low micromolar range (IC_{50} HO-1 = 0.9±0.08). Interestingly, this compound also showed the ability to discriminate between the two isoforms, showing an IC_{50} value for HO-2 of 38±0.2 μM and selectivity index (S.I.) of 42. Thus, when compared to compound **1** (IC_{50} HO-1 = 1.00±0.05, IC_{50} HO-2 = 10.0±0.5), the introduction of the benzylamide function in the central aryl ring was able to maintain the inhibition potency, while increasing the selectivity index of ~4 folds. The effect of the remaining compounds on the HO-2 activity was not evaluated due to their low potency on HO-1.

From a structure activity relationship (SAR) point of view, the presence of a bulkier moiety, such as the benzhydryl (**7d**), adamantyl (**7c**), and 3-benzyl-phenyl (**7e**) led to higher IC_{50} values; this may be associated to low fitting or unfavourable positioning into the hydrophobic pockets of the enzyme. On the contrary, even small hydrophobic groups such as the phenyl ring (**7a**) did not lead to a good inhibitory potency, probably due to non-suitable spatial conformation into the enzyme pockets. It is important to notice that the benzyl moiety of compound **7b,** thanks to the additional methylene group, might have higher freedom to rotate and to reach and fit better into the hydrophobic pockets. As a rule of thumb, the presence of halogens at the 4-position of aryl rings as in compound **7f** usually ameliorate the hydrophobic interactions (Amata et al., 2017a). In the present case, the substitution with a chlorine group at the 4-position of the benzyl moiety led to a decreased affinity with the enzyme, probably due to space limitation reasons. This result also suggests that an equilibrium between rotational freedom and bulkiness should be provided for having better enzymatic inhibition. Finally, obtained data suggest that the presence of a iodine group in position 5 of the central aryl ring is preferred when compared to a phenyl group (**7b** vs **8b**). In addition, compounds **7a** and **7c** were also phenylated in that position, and even in these cases led to a higher IC_{50} value, suggesting the elongation of the western region with a phenyl group is detrimental for HO-1 inhibitory activity.

3.4. NCI-60 test

Given the promising HO-1 inhibitory activity and good selectivity between the two isoforms, compound **7b** (from now on called VP 21–04) was firstly screened in a panel of 60 tumoral cell lines by NCI (Bethesda, MD, USA) to elucidate its tumor type susceptibility. Among the 60, 17 showed at least 30 % reduction on cell proliferation when treated at a 10 μM dose (Fig. S20). The highest reduction of cell growth was observed in the melanoma cell line SK-MEL-5 and the breast cancer cell line MDA-MB-468, with a 78.4 % and 65.7 % growth reduction, respectively (Fig. S20). Interestingly, both cancer cell lines share the characteristic of being metastatic, and numerous studies have described the involvement of HO-1 in promoting metastatization (Jozkowicz et al., 2007; Luu Hoang et al., 2021; Was et al., 2006). Specifically, for melanoma cancer cells, it was reported that HO-1 overexpression potentiates melanoma aggressiveness, proliferation, augmenting also the angiogenic and metastatic potential both *in vitro* and *in vivo* in mices (Was et al., 2006). Moreover, HO-1 induction enhances melanosphere formation in SK-MEL-5 cells, while heme oxygenase 1 gene (HMOX1) silencing decreases the spheroid formation (Jasmer et al., 2020). The overexpression of HO-1 has been also reported on breast cancer cell lines. Specifically, Zhu et al., 2015 reported the MDA-MB-468 cell line presented 18.6-fold higher overexpression of HMOX-1 than non-malignant breast cell line (MCF-10A), and the highest among other malignant breast cell lines. Thus, the central role played by HO-1 in both SK-MEL-5 and MDA-MB-468 cell lines can explain the promising anti-proliferative activity showed by VP21-04 in NCI-60 test.

3.5. NLC formulation and characterization

Lipophilic and low soluble drugs, such as VP21-04, may suffer of low bioavailability due to drug precipitation, first pass elimination through cytochrome P450 (CYP) enzymes, or be susceptible to efflux transporters such as P-glycoprotein (P-gp), having poor *in vivo* prospect. To predict the pharmacokinetic profile of VP 21–04, an *in-silico* ADMET analysis was performed using the SwissADME tool (Swiss Institute of Bioinformatics, Lausanne, Switzerland). Results showed that compound VP21-04 respect druglikeness rules and presents no Pan Assay Interference Structures (PAINS) in the molecular structure, depicting features to be a promising drug candidate (Daina et al., 2017; Ghose et al., 1999; Lipinski, 2000; Veber et al., 2002) (Fig. S21). Moreover, it may have high gastrointestinal (GI) absorption, permeate the Blood Brain Barrier (BBB), and could avoid P-glycoprotein (P-gp) efflux pump (Fig. S21). Conversely, the compound possesses an *in-silico* water solubility (Log S) from moderately soluble to poorly soluble, a Log Kp of −6.71 cm/s (index of low skin permeability) and could be substrate of all CYP enzymes. The affinity for cytochromes P450 enzymes derives from the fact that CYP uses the heme as cofactor. Thus, the presence of the imidazole ring in the HO-1 inhibitors, which is essential for heme binding and enzyme inhibition, may make them susceptible to CYP metabolism and first pass hepatic metabolism. Moreover, the low aqueous solubility of the drug can decrease its bioavailability while compromising the achievement of therapeutic drug concentrations and, therefore, effectiveness.

To fully exploit the therapeutic potential of VP21-04 and overcome its potential limitations as highlighted by the *in-silico* ADMET study, the formulation of an appropriate nanoparticle formulation may be an efficient strategy to pursue. In this context, NLCs could offer protection to the drug from enzymatic degradation, increase bioavailability, allow passive targeting, may reducing also clearence and toxicity. Indeed, NLCs have been reported as a useful strategy to overcome P-gp proteins efflux pumps and CYP degradation (Estella-Hermoso de Mendoza et al., 2011; Khan et al., 2015; Nguyen et al., 2021). Regarding P-gp proteins, certain lipids and surfactant used for NLCs formulation have been reported as inhibitors. NLCs can also offer transcytosis mechanism of absorption, avoiding efflux pump clearance (Nguyen et al., 2022). On the other hand, NLCs can enhance drug circulation in lymphatic ducts, bypassing the liver and first pass hepatic metabolization. Indeed, tamoxifen (antitumoral drug used for breast cancer) loaded NLCs were able to reach lymphatic transport, increasing the oral bioavailability of the drug avoiding extensive hepatic metabolization (Shete et al., 2013). Considering the administration for metastatic melanoma and breast cancer eradication, NLCs can present several advantages. NLCs with 50 to 200 nm size, can allow efficient tumor passive targeting (Makeen et al., 2021). Indeed, nanoparticles can exploit the tumor microenvironment characteristics as higher vessels fenestrations, offering

targeting selectivity by means of the Enhanced Permeability and Retention (EPR) effect (Maeda et al., 2013). Moreover, the above-mentioned nanometer size is reported to be appropriate to avoid risk of capillary occlusions and reduce reticuloendothelial system (RES) uptake (Alghamdi et al., 2022; Rizwanullah et al., 2016). Interestingly, given the affinity of NLCs for lymphatic circulation, it can be an appropriate vehicle for lymphatic tumor metastasis, such as those observed in breast cancer and melanoma. However, NLCs can offer possibility also for topical and site-specific administrations. In fact, NLCs are reported to be suitable for skin administration, which may fit well with melanoma topical treatment and enhance drug skin permeability (Souto et al., 2020). Other than this, NLCs may be also directly administrated in accessible solid tumor such as breast cancer, allowing a local administration. Thus, seen all the advantages that NLCs can provide for anti-tumoral delivery, these carriers have been chosen as the drug delivery system to encapsulate VP 21–04. Specifically, for the formation of the present NLC a Labrasol ALF:Compritol ATO 888 50:50 mass ratio was chosen for the formation of the NLC, based on the calculated LogP of the drug and the hydrophilic-lipophilic balance (HLB) of the excipients. Lecithin and Tween 80 were used as surfactants, and the preparation was conducted using a high shear homogenization method similarly to already reported in the literature (Rouco et al., 2020). Blank NLCs were also formulated to better understand how the presence of the drug can influence the nanoparticle performances and have been used as control. To assess the reproducibility of the drug loaded nanoparticles, three batches were prepared in different days and using different stock solutions (NLC 21–04 Batch 1, 2, and 3). After formulation, the filtrated nanoparticle dispersions were analyzed to determine the mean size, PDI and Z potential of both NLC 21–04 and blank NLC (Table 2). The results showed very similar data for all the formulated batches, confirming the formulation process is reproducible and robust (Fig. S22 and S23). Moreover, the overall NLC 21–04 mean size, 102.3±8.31 nm, and mean PDI, 0.21, confirmed the correct formation of a homogeneous nanoparticle system. Very similar negative Z potential was found in all the batches (mean −17.59 ± 1.354), indicative of a potentially good colloidal stability of the systems, in which the formation of aggregates can be prevented by negative repulsive forces. Interestingly, the absence of drug led to nanoparticles of higher size the (156.5±14.15) indicating the drug may play a role into lipids interactions and assembling, which are reflected by the final size.

UV–vis analysis was conducted on the formulated NPs to confirm the amount of drug loaded into the nanoparticle system, and also visualize how absorbance profile of the drug can vary before and after encapsulation. The absorption profile of NLC 21–04 and Blank NLC resulted to be different at the same concentration (50 μL/mL in DDW), showing the presence of a curve around 300 nm for NLC21-04, which represents the maximum absorption peak of the drug (Fig. 2A-1 and Fig. 2A-2). Nevertheless, both spectra are influenced by scattering phenomena due to the dispersion of the nanoparticles in water. A significant difference was seen after NLCs dissolution in ACN, allowing drug release (Fig. 2A-2). Indeed, after vortex and centrifugation, the free-drug present in the supernatant showed a clear peak at 300 nm, following the same absorption behaviour as the non-encapsulated drug spectra used as control, proving the suitable drug loading calculation (Fig. 2A-2 and Fig. 2A-3).

Table 2
Size, PDI, Z. pot, loading % and E.E % of the nanoparticle systems. Data are shown as the mean of triplicate experiments.

Sample	Size	PDI	Z Pot.	Loading (% w/w)	E.E (%)
NLC21-04 batch 1	107 ±1.66	0.212	−18.87 ± 0.90	1.33	79.6
NLC 21–04 batch 2	108.5 ±1.62	0.210	−16.34 ± 1.27	1.18	70
NLC 21–04 batch 3	91.5 ±2.00	0.220	−17.56 ± 0.31	1.25	75.16
Mean of all NLC21-04 batches	102.3 ±8.31	0.214	−17.59 ± 1.35	1.25±0.07	74.92 ±4.8
Mean all Blank NLC batches	156.5 ±14.15	0.129	–22.51 ± 2.4	–	–

Successively, a stability study was conducted on the loaded nanoparticles to verify the system stability over time in DDW at different storage temperatures (4 °C, r.t, and 37 °C) (Fig. 2B). The results showed a different behaviour, depending on the storage temperature. NLC 21–04 stored at 37 °C, showed a slight increase in size and PDI over time, while the Z potential was more negative than at the t = 0. Indeed, a higher size population was observed maybe due to aggregation phenomena (Fig. S24D). In addition, also a lower population size around 30 nm was observed after 4 days of storage, that could be attributable to NPs disassembly. A similar behaviour was seen for NLC 21–04 stored at r.t., but the instability appeared after 7 days of storage (Fig. S24B). Anyway, the initial nanoparticle population was still highly present in both dispersions, with a 96.82±5.5 % and 97.58±2.13 % abundance for the one stored at 37 °C and r.t., respectively. Differently, the NPs stored at 4 °C presented outstanding stability over 30 days, showing very similar size, PDI, and Z potential that those at t0, and not presenting any sub-population or aggregates (Fig. S24D).

To further validate the data obtained by DLS, a shorter stability study was performed by UV–vis analysis. In this case, a 50 μL/mL dispersion of NLC 21–04 in DDW was stored at 4 °C, r.t., and 37 °C for 7 days and analyzed at fixed timepoints. The obtained results agreed with the ones obtained by DLS. Indeed, the NPs system proved to be stable at 37 °C only for 4 days, showing higher scattering phenomena at day 7, which may be synonym of aggregation phenomena and/or NLC disassembly leading to a lower population size, as previously observed by DLS analysis (Fig. 2C). The same tendency was seen in the dispersion stored at r.t., where instability appeared after 7 days of storage, but with lower scattering than at 37 °C (Fig. 2C). On the other hand, the nanoparticle system proved to be stable at all timepoints when stored at 4 °C, showing similar absorption/scattering spectra along all the analysis (Fig. 2C).

Thus, the conducted DLS and UV–vis stability studies confirmed the NLCs stability over time, especially when stored at 4 °C. These data are in agreement with literature, where it has been demonstrated how NLCs alone can be stable for periods ≥1 year when stored at 4 °C (Gerhardt et al., 2022). An optimal stability was also observed for loaded NLCs. Indeed, Lekhani *et al.* reported that curcumin loaded NLCs can be stable for over a period of 3 month at 4 °C. However, aggregation phenomena and curcumin degradation were present at 25 °C (Lakhani et al., 2018).

Moreover, TEM analysis was conducted to visualize NLC 21–04 structure and morphology, to confirm the DLS size data. The collected images showed NLC 21–04 depicted a monodisperse size distribution around 100 nm, further validating the data obtained by DLS. Moreover, the nanoparticle showed a spherical shape, with a relatively smooth surface, which is the results of a correct lipid self-assembly during high shear homogenization process and reduced surface tension given by Tween® 80 and lecithin (Fig. 2D). These data agree with previously reported literature, where for NLCs a monodisperse spherical shape system is usually described (Garbuzenko et al., 2019; Ortiz et al., 2021). A nanoparticle size below 200 nm is reported to have a satisfactory passive targeting ability thanks to the EPR effect (Olerile et al., 2017). In addition, spherical particle sizes of <200 nm reduces RES system uptake, prolonging plasma circulation time, facilitating cellular uptake and internalization *via* clathrin or caveolae-mediated endocytosis (Yu et al., 2020). Thus, the obtained data suggests the developed NLC 21–04 can be suitable for the antitumoral aim of the study.

3.6. In vitro antiproliferative cells viability assay on melanoma and breast cancer cells

Given the promising growth inhibition showed by VP21-04, further investigations were conducted on SK-MEL-5 (melanoma) and MDA-MB-

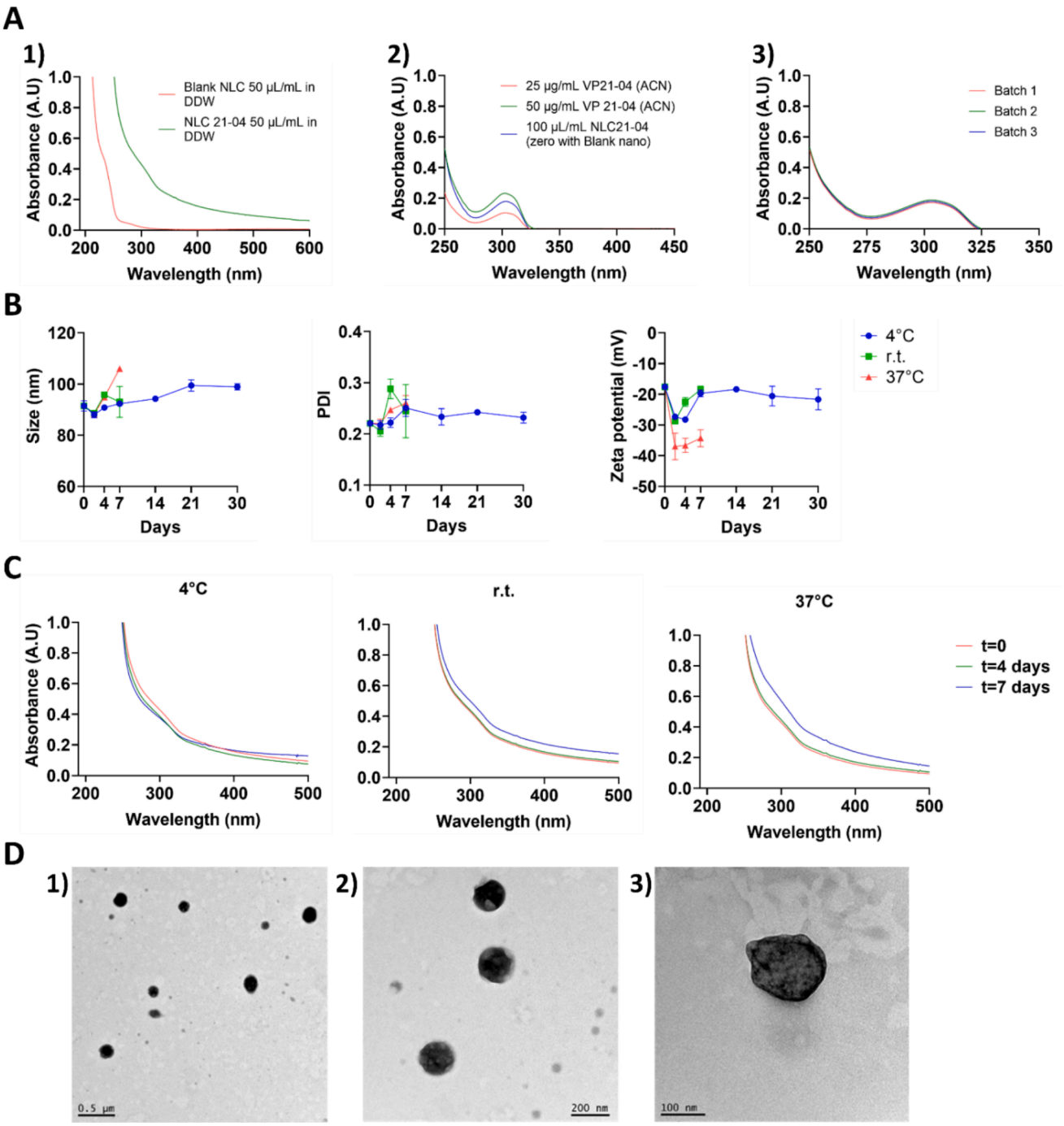

Fig. 2. Panel A) UV–vis analysis: 1) UV–vis profile of 50 µL/mL in DDW of Blank NLC vs NLC 21–04. 2) Uv–vis profile of VP21-04 in ACN vs VP21-04 released after NPs rupture in ACN. 3) UV–vis profile of VP21-04 released after NPs rupture for loading quantification in three different formulated batches. Panel B) DLS stability study of NLC 21–04 stored at different temperatures: Size, PDI, and Zeta potential of the NLC 21–04 stored at 4 °C, r.t., and 37 °C for 30 days (the analysis of the NPs stored at r.t. and 37 °C was stopped after 7 days). Panel C) UV–vis stability study of NLC 21–04 stored at 4 °C, r.t., and 37 °C for 7 days. All UV–vis measurements were done using a 1 cm path length quartz cells. Panel D) TEM images of NLC 21–04. 1) magnification was set at 3,000X; 2) magnification was set at 8,000X; 3) magnification was set at 20,000X.

468 (breast cancer) to evaluate the ability of the compound to reduce the viability of tumoral cells as free-drug and encapsulated in NLC. To this extent, Alamar blue cell viability assay has been performed at different concentrations (5, 10, 25, and 50 µM) after 24 and 48 h of exposure to VP21-04 and NLC21-04. The obtained data underlined the ability of VP21-04 in reducing the viability of both tumoral cell lines, with better results after 48 h treatment (Fig. 3A and B). Specifically, in MDA-MB-468, VP21-04 25 µM and 50 µM concentrations produced a cell survival rate of 56.8±5.1 % and 32.8±7.5 % after 24 h treatment, respectively, with further reduction after 48 h, where the same conditions produced a cell survival rate of 32.6±11.6 % and 11.6±6.7 %, respectively (Fig. 3A). Similarly, SK-MEL-5 cells treated with VP21-04 showed a marked reduction of cell viability at 50 µM after 24 h and 48 h with a 11.6±7.2 % and 0.8±0.7 %, cell survival rate, respectively. However, at lower concentration, 25 µM, the cell viability was 63.9±12 % after 24 h, while it was 37.8±14.2 % after 48 h (Fig. 3B). Thus, the results suggest that a 50 µM concentration massively reduce cell viability of the two cell lines, after 48 h; while a concentration of 25 µM

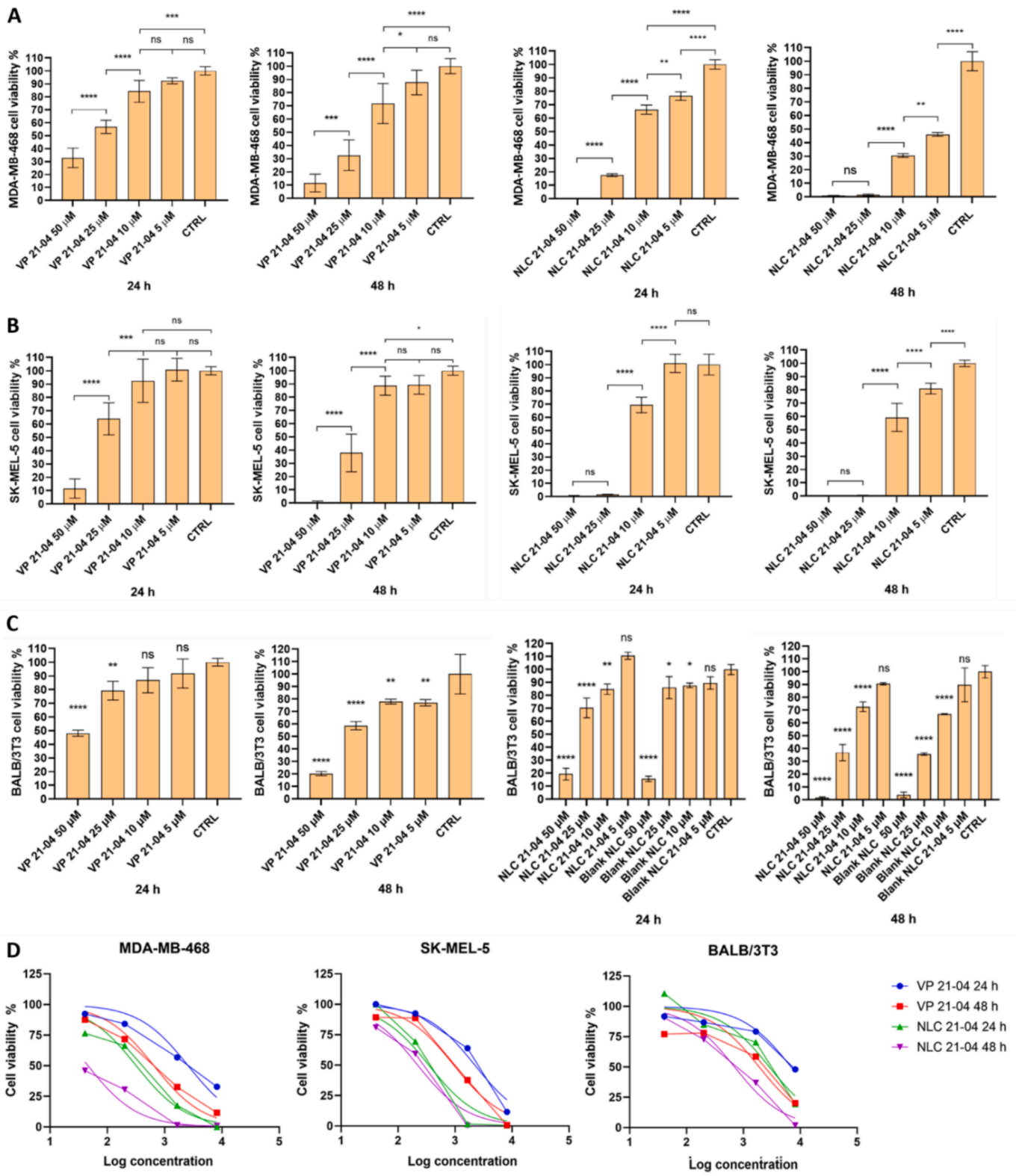

Fig. 3. A) MDA-MB-468 cell viability after 24 h and 48 h treatment with compound VP21-04 and NLC 21–04. B) SK-MEL-5 cell viability after 24 h and 48 h treatment with compound VP21-04 and NLC 21–04. C) BALB/3T3 cell viability after 24 h and 48 h treatment with compound VP21-04, NLC 21–04, and Blank NLC. One-way ANOVA statistical analysis: 0.1234 (ns), 0.0332 (*), 0.0021 (**), 0.0002 (***), <0.0001 (****). For VP 21–04 testing, the CTRL was 0.1 % v/v DMSO, while for NLC 21–04 and Blank NLC testing the CTRL was pure culture media. All the tests were performed using n = 5 replicates per conditions, and the shown data are the mean of three different experiments. D) LC_{50} graphs for VP 21–04 and NLC 21–04 in BALB/3T3, MDA-MB-468, and SK-MEL-5 cell lines.

can lead to a decrease of >50 % cell viability after 48 h. Conversely, a 10 μM concentration showed a cell viability reduction of <50 % in both cell lines. Regarding the NLC 21–04 antitumoral activity, dilutions of the nanoparticles in culture media were done to produce the equivalent free-drug concentration (5, 10, 25, and 50 μM) to have a direct comparison. The results showed no tumor cell survival at 50 μM after 24 h in both cell lines. In addition, also a massive reduction was seen for cells treated with 25 μM NLC after 24 h, especially in SK-MEL-5, with a massive cell death after 48 h in both tumoral lines. Interestingly, MDA-MB-468 cell survival decreased from ~70 % at 10 μM after 24 h to ~ 30 % after 48 h with NLC21-04 treatment, while the same behaviour was not observed on SK-MEL-5 (Fig. 3 A and B). The obtained results point out the encapsulation of the drug into the nanoparticle system leads to a favourable effect, producing a higher antiproliferative activity than the free drug at both timepoints, being also able to produce a massive at 25 μM just after 24 h.

After evaluating the antiproliferative properties, the cytotoxic effect of VP 21–04 and NLC 21–04 were screened on fibroblast BALB/3T3 to evaluate toxic effects towards normal mammalian cells. The conditions previously described were used for this analysis. The data obtained for the free-drug VP21-04 evidenced a cell viability of ~50 % at 50 μM, with a more marked toxic effect after 48 h exposure (~20 %). However, the cell compatibility of the 25 μM treatment was acceptable after 24 h treatment (~80 %), but was lowered to ~60 % at 48 h. Other concentrations proved to possess good cell compatibility, with a cell survival rate >70 % (Fig. 3C). Considering that the tested breast cancer and melanoma cell phenotypes are both metastatic tumors with a limited patient survival rate, high recurrence, and poor prognosis, the use of the free-drug itself may be still a profitable treatment strategy. As commonly known, chemotherapies usually possess a narrow therapeutic window and therapeutic and toxic effect are, in most of the cases and unfortunately, opposite sides of the same coin. Hence, given the poor alternatives present today in clinics for the treatment of the two tumors, the synthesized compound VP21-04 can represent an important tool of reference to further characterize the role the HO-1 within these two tumors (Greish et al., 2018a; Switzer et al., 2022).

NLC 21–04 showed high toxicity at 50 μM at both timepoints. However, an acceptable cytocompatibility was observed at 25 μM at 24 h with a cell viability value of ~70 %, while a higher toxic effect was reported after 48 h of exposure at the same concentration. Equally, a 10 μM concentration showed high cytocompatibility at 24 h and 48 h (≥70), and interestingly, at this concentration the cell viability of MDA-MB-468 was decreased by ~70 % at 48 h. On the other hand, only a reduction of ~40 % was seen for SK-MEL-5 at 10 μM concentration after 48 h, showing lower antitumoral efficacy than the one achieved with breast cancer, but still leading to an important reduction maintaining safety (Fig. 3C). Thus, other than showing better antiproliferative activity, NLC 21–04 possesses higher cytocompatibility than the free-drug, having a wider therapeutic index (Fig. 3D and Table 3). It is important to underline that, thanks to the NLC encapsulation, higher selectivity towards the tumor can be achieved thanks the passive tumor targeting and EPR effect (Alghamdi et al., 2022; Maeda et al., 2013). Other than allowing passive targeting, nanoparticles can enhance drug penetration into the tumor cell, efficiently releasing their cargo inside. As previously mentioned, the spherical shape and the optimal size showed by NLC-21 04 will favour the drug internalization *via* endocytosis, making easier for the drug to overcome the biological barriers, concentrate into the cell, and inhibit its final target (HO-1) (Mazumdar et al., 2021). Moreover, in case of drug resistance efflux mechanism, NLCs could bypass the binding to efflux pumps, improving the intracellular drug accumulation (Kapse-Mistry et al., 2014).

Moreover, the combination of several factors, such as VP21-04 selectivity towards HO-1, the overexpression of the enzyme into the tumoral cells, the NLC-21 04 wider therapeutic window, and enhanced selectivity thanks to passive targeting can even lower the side toxicity of the system, increasing the chance of a successful therapeutic opportunity.

Table 3
LC_{50} and Therapeutic Index (T.I) of VP21-04 and NLC 21–04. T.I was calculated using the following formula: T.I = Mean LC_{50} healthy cells/Mean LC_{50} tumoral cells.

Data	LC_{50} BALB/3T3	LC_{50} MDA-MB-468	LC_{50} SK-MEL-5	T.I MDA-MB-468	T.I SK-MEL-5
VP 21–04 24 h	51.91 ±1.57	30.72±6.43	28.10 ±6.42	1.69	1.84
VP 21–04 48 h	24.32 ±2.29	16.52±5.96	20.54 ±4.72	1.47	1.18
NLC 21–04 24 h	32.03 ±3.85	12.13±0.92	11.39 ±0.45	2.64	2.81
NLC 21–04 48 h	16.99 ±1.97	4.82±0.19	10.55 ±1.48	3.52	1.61

3.7. *In ovo* antitumoral testing

Despite *in vitro* 2D antitumoral studies can offer a rapid screening of tumoral cell susceptibility to a certain compound or formulation, they unfortunately lack tumor complexity when compared to the clinical set up. Indeed, *in vitro* cancer cells grow in a 2D hard surface, which cannot replicate the complex 3D architecture and microenvironment of the tumor (Kitaeva et al., 2020). The absence of Extracellular Matrix (ECM) as well as no blood supply modified the secretion biochemical signals that crucially influence cell behaviour, spreading, and survival (Walker et al., 2018). Thus, even if *in vitro* studies provide a good first step in testing, they do not offer comprehensive information about the antitumoral effect. These limitations can be overcome by *in ovo* test, translating the study from 2D to 3D (Miebach et al., 2022). Once the efficacy of NLC 21–04 in reducing cancer cell viability *in vitro* was demonstrated, further investigation was conducted *in ovo* to test the ability of the formulation in reducing tumoral growth in living chicken embryo. The *in ovo* CAM test represents a low cost, highly reliable, reproducible, and efficient alternative to animal experimentation, and can be helpful in reducing, refining, and replacing animals, sticking with the current recommendation of the European Chemical Agency (ECHA) of avoiding unnecessary testing (Miebach et al., 2022). Under the Directive 2010/63/EU (Directive 2010/63, (2010)), the CAM assay is not considered an animal experiment, since the embryo is not considered a living animal until Embrionic Day (ED) 17, and the Institutional Animal Care and Use Committee (IACUC) and the USA National Institutes of Health established that the chick embryo is not able to experience pain cause the CAM is not innervated (Kundeková et al., 2021). Moreover, since the embryo is an immunodeficient host, the engrafting of tumoral cells on the CAM can be performed with high efficiency and without species-specific restrictions (Miebach et al., 2022). Tumor grafting in the *in ovo* CAM has been demonstrated to be an advanced model that can overcome the limitation of 2D *in vitro* cell testing. Cancer is a complex disease, and as such requires adequate mimicking of the complex tumor microenvironment for truly establish the potentiality of new anticancer treatment. The vessels formation around the grafted tumor and the presence of the extracellular matrix in which tumoral cells can be enclosed (e.g., Matrigel), can recreate a complex bio-mimicry 3D structure of the tumor (Lokman et al., 2012).

For the present experiment, the MDA-MB-468 tumoral cell line was elected, given the higher therapeutic index showed *in vitro* by NLC 21–04. Before grafting, the tumoral cells were stained with the CellTracker™ Green CMFDA to allow visualization of the grafted tumor onto the CAM by fluorescence. The tumor graft was performed at the ED 7, with or without treatments (25 and 10 μM of NLC 21–04). Blank NLC were also tested at the same concentration to evidence the potential effects of the drug. A preliminary macroscopic visual analysis revealed a correct tumor grafting and formation, similarly to previously reported procedures in literature (Li et al., 2015; Mitrevska et al., 2023). All the

embryos were viable and were growing correctly, showing no sign of toxicity and hemolysis for the used treatments (Fig. S25). Successively, images of the grafting site were taken using a stereomicroscope in both brightfield and fluorescence mode, and fluorescence intensity was calculated. The obtained images and results evidenced that both the 25 and 10 μM dose were able to significatively reduce the tumoral growth of MDA-MB-468 cells when compared to control. Indeed, the mean fluorescence intensity was reduced by 28 % for 10 μM NLC 21–04 and by 63 % for 25 μM NLC 21–04 (Fig. 4). It is important to notice that the Blank NLC were not effective in reducing tumoral growth, showing a similar mean fluorescence intensity than control, underlining the importance and the huge impact that the drug can have on the grafted tumor. On the other hand, neither of the treatments modified the tumor angiogenesis (Fig. S26). Thus, NLC 21–04 demonstrated to possess a potent antitumoral activity against TNBC *in ovo*, presenting high beneficial effect over toxicity; Moreover, comparative literature analysis on MDA-MB-468 *in ovo* grafted cells show that NLC 21–04 can have similar potency to Doxorubicin (drug used to manage TNBC) when tested *in ovo,* but without showing the high toxicity and hemolysis given by Doxorubicin (Asariha et al., 2022).

In ovo models can be suitable to study tumor growth, angiogenesis, and drug responses, offering advantages over mammalian animal models as allows a cost-effective fast analysis of the antitumoral activity of new molecules and drug delivery systems with reduced ethical concerns. However, these models still present some limitations when compared to *in vivo* studies, such as: i) impossibility to mimic the complex interactions between the tumor and the immune system; ii) impossibility to replicate the organ-specific context of tumors (such as

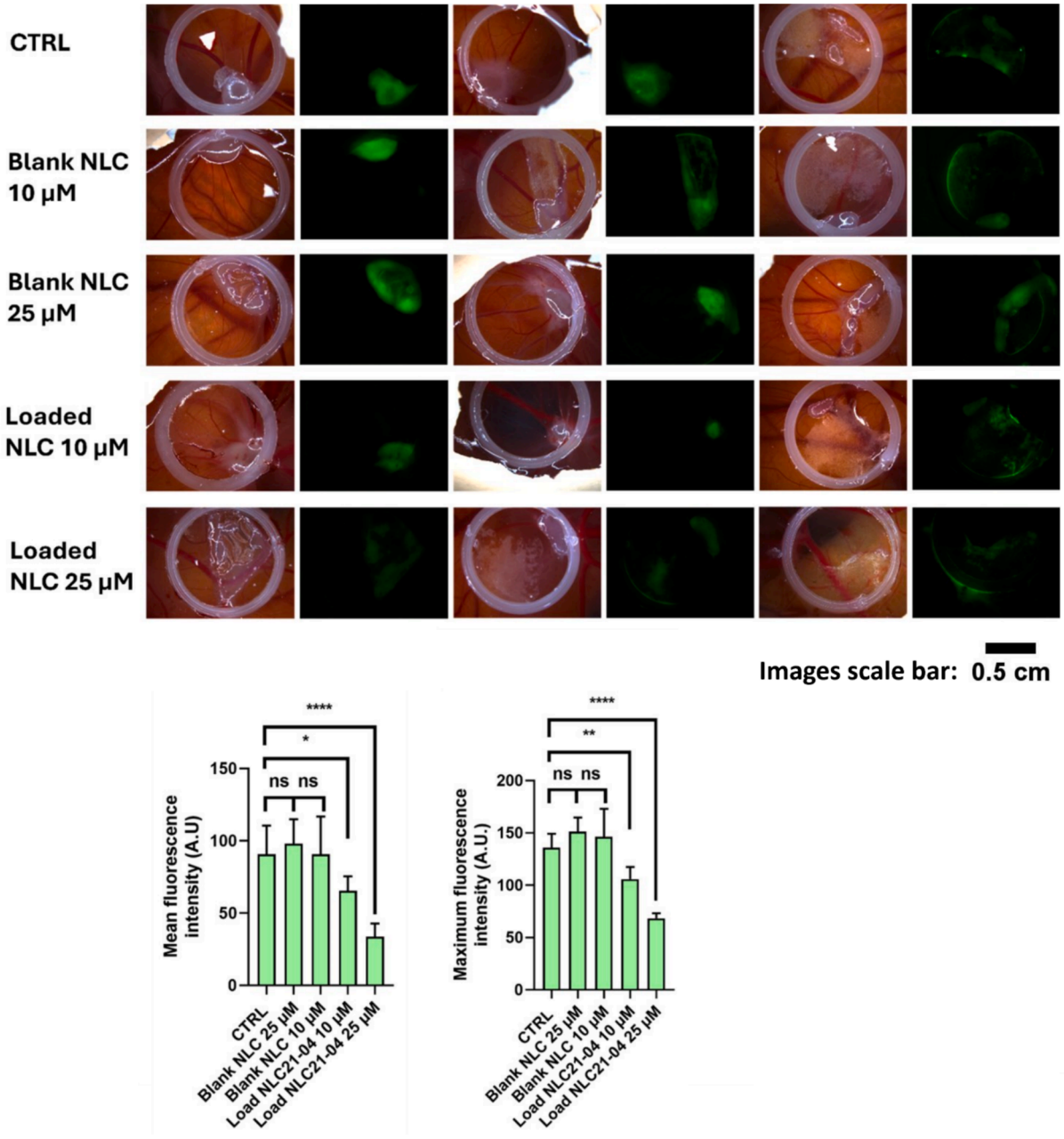

Fig. 4. Chick CAM grafted with MDA-MB-468 cells tagged with CellTracker™ Green CMFDA fluorescent probe with or without NLC 21–04 NPs or Blank NPs (n = 3). The images were taken using a stereomicroscope using a 10x magnification. The PCL rings possess an inner diameter of 1 cm. Quantification of the mean fluoresce intensity and maximum fluorescence intensity were calculated by ImageJ software, in triplicate. One-way ANOVA: 0.1234 (ns), 0.0332 (*), 0.0021 (**), 0.0002 (***), <0.0001 (****).

liver, lung, or brain cancer); iii) tumors growing on the CAM membrane do not experience the level of oxygenation, nutrient supply, and pressure of mammalian organs; iv) reduced pharmacokinetic mimicry (e.g., no exposure of the treatment to metabolism); v) reduced study period and impossibility to study the effect of long-term drug exposure (Miebach et al., 2022). Therefore, the positive antitumoral results obtained in this study should be further confirmed in preclinical studies.

4. Conclusions

The present paper reports the rational design and chemical synthesis of a small focused series of HO-1 inhibitors. Crucial structural features have been combined to afford VP21-04 as potent HO-1 inhibitor, decreasing the affinity for the constitutive HO-2 isoform. More importantly, VP21-04 exhibited cytotoxic activity towards SK-MEL-5 and MDA-MB-468 cell lines both overexpressing HO-1. VP21-04 has been encapsulated in NLC to enhance its water solubility, and ADMET profile. Analytical, spectroscopic, and morphological analysis of NLC21-04 demonstrated a suitable, reliable, and reproducible formulation procedure. Information on the size, morphology and colloidal stability confirmed a profile suitable for optimal passive EPR effect and low RES uptake. In addition, NLC 21–04 nanoparticles resulted to be stable at 4 °C until 4 weeks, demonstrating optimal storability.

More importantly, NLC 21–04 showed even stronger cytotoxic activity as well as wider therapeutic window than the parent free-compound towards metastatic SK-MEL-5 and MDA-MB-468 cells. Finally, as viable alternative to *in vivo* studies, CAM grafted with MDA-MB-468 cells were treated with NLC 21–04 and exhibited a marked reduction in tumor proliferation. Overall, this study led to the identification of VP21-04 as a new tool to manage HO-1 in metastatic aggressive cancers such as TNBC and melanoma, and its encapsulation in NLC represents a promising strategy to improve its biological effects. Thus, NLC 21–04 can be considered a promising and valid tool for potentially treating metastatic tumor with low patient survival rate (such as TNBC). Further *in vivo* and clinical studies may provide additional data to better understand the therapeutic applicability of the developed formulation. To date, the present NLC 21–04 efficiently combines novel drug discovery and appropriate nano-drug delivery systems.

CRediT authorship contribution statement

Nicola Filippo Virzì: Writing – review & editing, Writing – original draft, Visualization, Software, Methodology, Investigation, Formal analysis, Data curation, Conceptualization. **Carmen Alvarez-Lorenzo:** Writing – review & editing, Validation, Supervision, Resources, Project administration, Methodology, Funding acquisition, Formal analysis, Conceptualization. **Angel Concheiro:** Writing – review & editing, Supervision, Project administration, Funding acquisition, Conceptualization. **Valeria Consoli:** Writing – review & editing, Software, Methodology, Investigation, Formal analysis, Data curation. **Loredana Salerno:** Writing – review & editing, Supervision, Project administration, Funding acquisition, Conceptualization. **Luca Vanella:** Writing – review & editing, Supervision, Project administration, Funding acquisition, Conceptualization. **Valeria Pittalà:** Writing – review & editing, Software, Methodology, Investigation, Formal analysis, Data curation. **Patricia Diaz-Rodriguez:** Writing – review & editing, Writing – original draft, Visualization, Validation, Supervision, Project administration, Methodology, Investigation, Funding acquisition, Formal analysis, Conceptualization.

Declaration of competing interest

The authors declare the following financial interests/personal relationships which may be considered as potential competing interests: Valeria Pittala reports financial support was provided by Research Funding for University (Programma Ricerca di Ateneo). Patricia Diaz-Rodriguez reports financial support was provided by Spain Ministry of Science and Innovation. Patricia Diaz-Rodriguez reports financial support was provided by Government of Galicia. Patricia Diaz-Rodriguez reports financial support was provided by Interreg-POCTEP 2021–2027. Carmen Alvarez-Lorenzo is Editor of International Journal of Pharmaceutics. If there are other authors, they declare that they have no known competing financial interests or personal relationships that could have appeared to influence the work reported in this paper.

Acknowledgements

The authors wish to thank the National Cancer Institute Developmental Therapeutics Program (NCI/DTP) https://dtp.cancer.gov for providing screening data of compound VP 21-04 (**7b**). Part of the results showed in this paper have been achieved within the framework of Center for Advanced Preclinical *in vitro* Research (CAPiR) of University of Catania through project authorized by Ministry of Health: "Dosing of enzymatic activities in rat microsomes: evaluation of the effect of natural and synthetic molecules" (2023-2025, project code 1984F.N.FGE)".

Funding

This research was founded by Ministero Universitá e Ricerca (MUR) - Research Funding for University (Programma Ricerca di Ateneo) UNICT Pia.Ce.Ri 2020-2022 linea 2, project number 57722172126; Spain Ministerio de Ciencia e Innovación MCIN/AEI/10.13039/501100011033/FEDER, UE, [PID2021–127493OA-C22] and Xunta de Galicia [ED431C 2024/09], FEDER. Work partially financed by project IBEROS+[0072_IBEROS_MAIS_1_E] Interreg-POCTEP 2021-2027.

Appendix A. Supplementary data

Supplementary data to this article can be found online at https://doi.org/10.1016/j.ijpharm.2024.124997.

Data availability

Data will be made available on request.

References

Abraham, N.G., Kappas, A., 2008. Pharmacological and clinical aspects of heme oxygenase. Pharmacol Rev 60, 79–127.
Alghamdi, M.A., Fallica, A.N., Virzì, N., Kesharwani, P., Pittalà, V., Greish, K., 2022. The Promise of Nanotechnology in Personalized Medicine. J Pers Med 12.
Amata, E., Marrazzo, A., Dichiara, M., Modica, M.N., Salerno, L., Prezzavento, O., Nastasi, G., Rescifina, A., Romeo, G., Pittalà, V., 2017a. Comprehensive data on a 2D-QSAR model for Heme Oxygenase isoform 1 inhibitors. Data Brief 15, 281–299.
Amata, E., Marrazzo, A., Dichiara, M., Modica, M.N., Salerno, L., Prezzavento, O., Nastasi, G., Rescifina, A., Romeo, G., Pittalà, V., 2017b. Heme Oxygenase Database (HemeOxDB) and QSAR Analysis of Isoform1 Inhibitors. ChemMedChem 12, 1873–1881.
Asariha, M., Kiaie, S.H., Izadi, S.F.H.P., Fouladi, M.M., Gholamhosseinpour, 2022. Extended-release of doxorubicin through green surface modification of gold nanoparticles: in vitro and in ovo assessment. BMC Chem 16, 110.
Daina, A., Michielin, O., Zoete, V., 2017. SwissADME: a free web tool to evaluate pharmacokinetics, drug-likeness and medicinal chemistry friendliness of small molecules. Sci Rep 7, 42717.
Dennery, P.A., 2014. Signaling function of heme oxygenase proteins. Antioxid Redox Signal 20, 1743–1753.
Directive 2010/63. Directive (EU) 2010/63 of the European Parliament and of the Council of 22 September 2010 on the Protection of Animals Used for Scientific Purposes; European Union: Brussels, Belgium. 2010. 1-47.
https://dtp.cancer.gov/discovery_development/nci-60/default.htm.
Estella-Hermoso de Mendoza, A., Préat, V., Mollinedo, F., Blanco-Prieto, M.J., 2011. In vitro and in vivo efficacy of edelfosine-loaded lipid nanoparticles against glioma. J Control Release 156, 421–426.
Fallica, A.N., Sorrenti, V., D'Amico, A.G., Salerno, L., Romeo, G., Intagliata, S., Consoli, V., Floresta, G., Rescifina, A., D'Agata, V., Vanella, L., Pittalà, V., 2021. Discovery of Novel Acetamide-Based Heme Oxygenase-1 Inhibitors with Potent In Vitro Antiproliferative Activity. J Med Chem 64, 13373–13393.

Floresta, G., Fallica, A.N., Patamia, V., Sorrenti, V., Greish, K., Rescifina, A., Pittalà, V., 2021a. From Far West to East: Joining the Molecular Architecture of Imidazole-like Ligands in HO-1 Complexes. Pharmaceuticals (Basel) 14.
Floresta, G., Fallica, A.N., Salerno, L., Sorrenti, V., Pittalà, V., Rescifina, A., 2021b. Growing the molecular architecture of imidazole-like ligands in HO-1 complexes. Bioorg Chem 117, 105428.
Garbuzenko, O.B., Kuzmov, A., Taratula, O., Pine, S.R., Minko, T., 2019. Strategy to enhance lung cancer treatment by five essential elements: inhalation delivery, nanotechnology, tumor-receptor targeting, chemo- and gene therapy. Theranostics 9, 8362–8376.
Gerhardt, A., Voigt, E., Archer, M., Reed, S., Larson, E., Van Hoeven, N., Kramer, R., Fox, C., Casper, C., 2022. A flexible, thermostable nanostructured lipid carrier platform for RNA vaccine delivery. Mol Ther Methods Clin Dev 25, 205–214.
Ghose, A.K., Viswanadhan, V.N., Wendoloski, J.J., 1999. A knowledge-based approach in designing combinatorial or medicinal chemistry libraries for drug discovery. 1. A qualitative and quantitative characterization of known drug databases. J Comb Chem 1, 55–68.
Greish, K., Pittalà, V., Taurin, S., Taha, S., Bahman, F., Mathur, A., Jasim, A., Mohammed, F., El-Deeb, I.M., Fredericks, S., Rashid-Doubell, F., 2018a. Curcumin¯Copper Complex Nanoparticles for the Management of Triple-Negative Breast Cancer. Nanomaterials (basel) 8.
Greish, K.F., Salerno, L., Al Zahrani, R., Amata, E., Modica, M.N., Romeo, G., Marrazzo, A., Prezzavento, O., Sorrenti, V., Rescifina, A., Floresta, G., Intagliata, S., Pittalà, V., 2018b. Novel Structural Insight into Inhibitors of Heme Oxygenase-1 (HO-1) by New Imidazole-Based Compounds: Biochemical and In Vitro Anticancer Activity Evaluation. Molecules 23, 1209.
Grochot-Przeczek, A., Kotlinowski, J., Kozakowska, M., Starowicz, K., Jagodzinska, J., Stachurska, A., Volger, O.L., Bukowska-Strakova, K., Florczyk, U., Tertil, M., Jazwa, A., Szade, K., Stepniewski, J., Loboda, A., Horrevoets, A.J., Dulak, J., Jozkowicz, A., 2014. Heme oxygenase-1 is required for angiogenic function of bone marrow-derived progenitor cells: role in therapeutic revascularization. Antioxid Redox Signal 20, 1677–1692.
Heasman, S.A., Zaitseva, L., Bowles, K.M., Rushworth, S.A., Macewan, D.J., 2011. Protection of acute myeloid leukaemia cells from apoptosis induced by front-line chemotherapeutics is mediated by haem oxygenase-1. Oncotarget 2, 658–668.
Holbeck, S.L., Collins, J.M., Doroshow, J.H., 2010. Analysis of Food and Drug Administration-approved anticancer agents in the NCI60 panel of human tumor cell lines. Mol Cancer Ther 9, 1451–1460.
Intagliata, S., Salerno, L., Ciaffaglione, V., Leonardi, C., Fallica, A.N., Carota, G., Amata, E., Marrazzo, A., Pittalà, V., Romeo, G., 2019. Heme Oxygenase-2 (HO-2) as a therapeutic target: Activators and inhibitors. Eur J Med Chem 183, 111703.
Jasmer, K.J., Hou, J., Mannino, P., Cheng, J., Hannink, M., 2020. Heme oxygenase promotes B-Raf-dependent melanosphere formation. Pigment Cell Melanoma Res 33, 850–868.
Jozkowicz, A., Was, H., Dulak, J., 2007. Heme oxygenase-1 in tumors: is it a false friend? Antioxid Redox Signal 9, 2099–2117.
Kapse-Mistry, S., Govender, T., Srivastava, R., Yergeri, M., 2014. Nanodrug delivery in reversing multidrug resistance in cancer cells. Front Pharmacol 5, 159.
Khan, S., Baboota, S., Ali, J., Khan, S., Narang, R.S., Narang, J.K., 2015. Nanostructured lipid carriers: An emerging platform for improving oral bioavailability of lipophilic drugs. Int J Pharm Investig 5, 182–191.
Kitaeva, K.V., Rutland, C.S., Rizvanov, A.A., Solovyeva, V.V., 2020. Cell Culture Based in vitro Test Systems for Anticancer Drug Screening. Front Bioeng Biotechnol 8, 322.
Kozakowska, M., Ciesla, M., Stefanska, A., Skrzypek, K., Was, H., Jazwa, A., Grochot-Przeczek, A., Kotlinowski, J., Szymula, A., Bartelik, A., Mazan, M., Yagensky, O., Florczyk, U., Lemke, K., Zebzda, A., Dyduch, G., Nowak, W., Szade, K., Stepniewski, J., Majka, M., Derlacz, R., Loboda, A., Dulak, J., Jozkowicz, A., 2012. Heme oxygenase-1 inhibits myoblast differentiation by targeting myomirs. Antioxid Redox Signal 16, 113–127.
Kundeková, B., Máčajová, M., Meta, M., Čavarga, I., Bilčík, B., 2021. Chorioallantoic Membrane Models of Various Avian Species: Differences and Applications. Biology (basel) 10.
Kutty, R.K., Kutty, G., Rodriguez, I.R., Chader, G.J., Wiggert, B., 1994. Chromosomal localization of the human heme oxygenase genes: heme oxygenase-1 (HMOX1) maps to chromosome 22q12 and heme oxygenase-2 (HMOX2) maps to chromosome 16p13.3. Genomics 20, 513–516.
Lakhani, P., Patil, A., Taskar, P., Ashour, E., Majumdar, S., 2018. Curcumin-loaded Nanostructured Lipid Carriers for Ocular Drug Delivery: Design Optimization and Characterization. J Drug Deliv Sci Technol 47, 159–166.
Li, M., Pathak, R.R., Lopez-Rivera, E., Friedman, S.L., Aguirre-Ghiso, J.A., Sikora, A.G., 2015. The In Ovo Chick Chorioallantoic Membrane (CAM) Assay as an Efficient Xenograft Model of Hepatocellular Carcinoma. J vis Exp.
Lipinski, C.A., 2000. Drug-like properties and the causes of poor solubility and poor permeability. J Pharmacol Toxicol Methods 44, 235–249.
Lokman, N.A., Elder, A.S.F., Ricciardelli, C., Oehler, M.K., 2012. Chick chorioallantoic membrane (CAM) assay as an in vivo model to study the effect of newly identified molecules on ovarian cancer invasion and metastasis. Int J Mol Sci 13, 9959–9970.
Luu Hoang, K.N., Anstee, J.E., Arnold, J.N., 2021. The Diverse Roles of Heme Oxygenase-1 in Tumor Progression. Front Immunol 12, 658315.
Maeda, H., Nakamura, H., Fang, J., 2013. The EPR effect for macromolecular drug delivery to solid tumors: Improvement of tumor uptake, lowering of systemic toxicity, and distinct tumor imaging in vivo. Adv Drug Deliv Rev 65, 71–79.
Maines, M.D., 1997. The heme oxygenase system: a regulator of second messenger gases. Annu Rev Pharmacol Toxicol 37, 517–554.
Makeen, H.A., Mohan, S., Al-Kasim, M.A., Sultan, M.H., Albarraq, A.A., Ahmed, R.A., Alhazmi, H.A., Alam, M.I., 2021. Preparation, Characterization, and Anti-Cancer Activity of Nanostructured Lipid Carriers Containing Imatinib. Pharmaceutics 13.
Mazumdar, S., Chitkara, D., Mittal, A., 2021. Exploration and insights into the cellular internalization and intracellular fate of amphiphilic polymeric nanocarriers. Acta Pharm Sin B 11, 903–924.
Miebach, L., Berner, J., Bekeschus, S., 2022. In ovo model in cancer research and tumor immunology. Front Immunol 13, 1006064.
Mitrevska, K., Merlos Rodrigo, M.A., Cernei, N., Michalkova, H., Splichal, Z., Hynek, D., Zitka, O., Heger, Z., Kopel, P., Adam, V., Milosavljevic, V., 2023. Chick chorioallantoic membrane (CAM) assay for the evaluation of the antitumor and antimetastatic activity of platinum-based drugs in association with the impact on the amino acid metabolism. Mater Today Bio 19, 100570.
Morales, A.A., Gutman, D., Cejas, P.J., Lee, K.P., Boise, L.H., 2009. Reactive oxygen species are not required for an arsenic trioxide-induced antioxidant response or apoptosis. J Biol Chem 284, 12886–12895.
Mucha, O., Podkalicka, P., Mikulski, M., Barwacz, S., Andrysiak, K., Biela, A., Mieczkowski, M., Kachamakova-Trojanowska, N., Ryszawy, D., Białas, A., Szelążek, B., Grudnik, P., Majewska, E., Michalik, K., Jakubiec, K., Bień, M., Witkowska, N., Gluza, K., Ekonomiuk, D., Sitarz, K., Gałęzowski, M., Brzózka, K., Dubin, G., Józkowicz, A., Dulak, J., Łoboda, A., 2019. Development and characterization of a new inhibitor of heme oxygenase activity for cancer treatment. Arch Biochem Biophys 671, 130–142.
Na, H.K., Surh, Y.J., 2014. Oncogenic potential of Nrf2 and its principal target protein heme oxygenase-1. Free Radic Biol Med 67, 353–365.
Nguyen, T.T., Duong, V.A., Maeng, H.J., 2021. Pharmaceutical Formulations with P-Glycoprotein Inhibitory Effect as Promising Approaches for Enhancing Oral Drug Absorption and Bioavailability. Pharmaceutics 13.
Nguyen, V.H., Thuy, V.N., Van, T.V., Dao, A.H., Lee, B.-J., 2022. Nanostructured lipid carriers and their potential applications for versatile drug delivery via oral administration. OpenNano 8, 100064.
Nitti, M., Piras, S., Marinari, U.M., Moretta, L., Pronzato, M.A., Furfaro, A.L., 2017. HO-1 Induction in Cancer Progression: A Matter of Cell Adaptation. Antioxidants (Basel) 6.
Olerile, L.D., Liu, Y., Zhang, B., Wang, T., Mu, S., Zhang, J., Selotlegeng, L., Zhang, N., 2017. Near-infrared mediated quantum dots and paclitaxel co-loaded nanostructured lipid carriers for cancer theragnostic. Colloids Surf B Biointerfaces 150, 121–130.
Ortiz, A.C., Yañez, O., Salas-Huenuleo, E., Morales, J.O., 2021. Development of a Nanostructured Lipid Carrier (NLC) by a Low-Energy Method, Comparison of Release Kinetics and Molecular Dynamics Simulation. Pharmaceutics 13.
Pae, H.O., Oh, G.S., Choi, B.M., Chae, S.C., Chung, H.T., 2003. Differential expressions of heme oxygenase-1 gene in CD25- and CD25+ subsets of human CD4+ T cells. Biochem Biophys Res Commun 306, 701–705.
Rahman, M.N., Vlahakis, J.Z., Vukomanovic, D., Lee, W., Szarek, W.A., Nakatsu, K., Jia, Z., 2012. A novel, "double-clamp" binding mode for human heme oxygenase-1 inhibition. PLoS One 7, e29514.
Rahman, M.N., Vukomanovic, D., Vlahakis, J.Z., Szarek, W.A., Nakatsu, K., Jia, Z., 2013. Structural insights into human heme oxygenase-1 inhibition by potent and selective azole-based compounds. J R Soc Interface 10, 20120697.
Rizwanullah, M., Ahmad, J., Amin, S., 2016. Nanostructured Lipid Carriers: A Novel Platform for Chemotherapeutics. Curr Drug Deliv 13, 4–26.
Rouco, H., Diaz-Rodriguez, P., Gaspar, D.P., Gonçalves, L.M.D., Cuerva, M., Remuñán-López, C., Almeida, A.J., Landin, M., 2020. Rifabutin-Loaded Nanostructured Lipid Carriers as a Tool in Oral Anti-Mycobacterial Treatment of Crohn's Disease. Nanomaterials (Basel) 10.
Ryter, S.W., Alam, J., Choi, A.M., 2006. Heme oxygenase-1/carbon monoxide: from basic science to therapeutic applications. Physiol Rev 86, 583–650.
Salerno, L., Pittalà, V., Romeo, G., Modica, M.N., Siracusa, M.A., Di Giacomo, C., Acquaviva, R., Barbagallo, I., Tibullo, D., Sorrenti, V., 2013. Evaluation of novel aryloxyalkyl derivatives of imidazole and 1,2,4-triazole as heme oxygenase-1 (HO-1) inhibitors and their antitumor properties. Bioorg Med Chem 21, 5145–5153.
Salerno, L., Pittalà, V., Romeo, G., Modica, M.N., Marrazzo, A., Siracusa, M.A., Sorrenti, V., Di Giacomo, C., Vanella, L., Parayath, N.N., Greish, K., 2015. Novel imidazole derivatives as heme oxygenase-1 (HO-1) and heme oxygenase-2 (HO-2) inhibitors and their cytotoxic activity in human-derived cancer cell lines. Eur J Med Chem 96, 162–172.
Salerno, L., Floresta, G., Ciaffaglione, V., Gentile, D., Margani, F., Turnaturi, R., Rescifina, A., Pittalà, V., 2019. Progress in the development of selective heme oxygenase-1 inhibitors and their potential therapeutic application. Eur J Med Chem 167, 439–453.
Schaefer, B., Behrends, S., 2017. Translocation of heme oxygenase-1 contributes to imatinib resistance in chronic myelogenous leukemia. Oncotarget 8, 67406–67421.
Seo, G.S., Jiang, W.Y., Chi, J.H., Jin, H., Park, W.C., Sohn, D.H., Park, P.H., Lee, S.H., 2015. Heme oxygenase-1 promotes tumor progression and metastasis of colorectal carcinoma cells by inhibiting antitumor immunity. Oncotarget 6, 19792–19806.
Shete, H., Chatterjee, S., De, A., Patravale, V., 2013. Long chain lipid based tamoxifen NLC. Part II: pharmacokinetic, biodistribution and in vitro anticancer efficacy studies. Int J Pharm 454, 584–592.
Shoemaker, R.H., 2006. The NCI60 human tumor cell line anticancer drug screen. Nat Rev Cancer 6, 813–823.
Souto, E.B., Baldim, I., Oliveira, W.P., Rao, R., Yadav, N., Gama, F.M., Mahant, S., 2020. SLN and NLC for topical, dermal, and transdermal drug delivery. Expert Opin Drug Deliv 17, 357–377.
Switzer, B., Puzanov, I., Skitzki, J.J., Hamad, L., Ernstoff, M.S., 2022. Managing Metastatic Melanoma in 2022: A Clinical Review. JCO Oncol Pract 18, 335–351.

Veber, D.F., Johnson, S.R., Cheng, H.Y., Smith, B.R., Ward, K.W., Kopple, K.D., 2002. Molecular properties that influence the oral bioavailability of drug candidates. J Med Chem 45, 2615–2623.
Vlahakis, J.Z., Kinobe, R.T., Bowers, R.J., Brien, J.F., Nakatsu, K., Szarek, W.A., 2005. Synthesis and evaluation of azalanstat analogues as heme oxygenase inhibitors. Bioorg Med Chem Lett 15, 1457–1461.
Vlahakis, J.Z., Lazar, C., Roman, G., Vukomanovic, D., Nakatsu, K., Szarek, W.A., 2012. Heme oxygenase inhibition by α-(1H-imidazol-1-yl)-ω-phenylalkanes: effect of introduction of heteroatoms in the alkyl linker. ChemMedChem 7, 897–902.
Walker, C., Mojares, E., Del Río Hernández, A., 2018. Role of Extracellular Matrix in Development and Cancer Progression. Int J Mol Sci 19, 3028.
Was, H., Cichon, T., Smolarczyk, R., Rudnicka, D., Stopa, M., Chevalier, C., Leger, J.J., Lackowska, B., Grochot, A., Bojkowska, K., Ratajska, A., Kieda, C., Szala, S., Dulak, J., Jozkowicz, A., 2006. Overexpression of heme oxygenase-1 in murine melanoma: increased proliferation and viability of tumor cells, decreased survival of mice. Am J Pathol 169, 2181–2198.
Wegiel, B., Hedblom, A., Li, M., Gallo, D., Csizmadia, E., Harris, C., Nemeth, Z., Zuckerbraun, B.S., Soares, M., Persson, J.L., Otterbein, L.E., 2014. Heme oxygenase-1 derived carbon monoxide permits maturation of myeloid cells. Cell Death Dis 5, e1139.
Yi, L., Ragsdale, S.W., 2007. Evidence that the heme regulatory motifs in heme oxygenase-2 serve as a thiol/disulfide redox switch regulating heme binding. J Biol Chem 282, 21056–21067.
Yu, W., Liu, R., Zhou, Y., Gao, H., 2020. Size-Tunable Strategies for a Tumor Targeted Drug Delivery System. ACS Cent Sci 6, 100–116.
Zhu, X.F., Li, W., Ma, J.Y., Shao, N., Zhang, Y.J., Liu, R.M., Wu, W.B., Lin, Y., Wang, S.M., 2015. Knockdown of heme oxygenase-1 promotes apoptosis and autophagy and enhances the cytotoxicity of doxorubicin in breast cancer cells. Oncol Lett 10, 2974–2980.